

**The Stress State Identification of Critical Steel Bridge Components using  
Nonlinear Acoustics**

BY

JAMES BITTNER

B.S. (Michigan Technological University) 2008

THESIS

Submitted in partial fulfillment of the requirements  
for the degree of Masters of Science in Civil Engineering  
in the Graduate College of the  
University of Illinois at Chicago, 2012

Chicago, Illinois

Defense Committee:

Dr. Didem Ozevin, Chair and Advisor  
Dr. Farhad Ansari, Department Head, Civil & Materials Engineering  
Dr. Eduard Karpov, Civil & Materials Engineering

This thesis is dedicated to my wife, Katie.

## ACKNOWLEDGMENTS

This investigation was supported by the National Academics, National Academy of Sciences NCHRP IDEA program under Contract No. NCHRP-158 entitled, The Identification of Stress State of Critical Bridge Components using Nonlinear Acoustics. The support from the sponsor is gratefully acknowledged. Any opinions, findings, and conclusions or recommendations expressed in this thesis are those of the authors and do not necessarily reflect the views of the organizations acknowledged above. Also, I would like to thank the Civil & Materials Department and the Physics Department at University of Illinois at Chicago for providing the opportunities and funding that made attending graduate school possible.

I would like to express my heartfelt gratitude to all of the individuals who aided in the construction of this thesis. Firstly my advisor, Dr. Ozevin has been a solid foundation of leadership and inspiration. From her example I have grown by setting goals high and achieving each one through efficient preparation and hard work. I am truly grateful to have had the opportunity to work with such a devoted advisor. Secondly my thesis committee, Dr. Ansari and Dr. Karpov for each of their willingness to review and provide invaluable suggestions.

The product of research is primarily the results of community. From this I would like to thank my community within the laboratory and beyond. Many thanks to Hossain, Zahra, Hazim and Lu for providing an invaluable sounding board. Also, I would like to thank Dr. Ansari, Dr. Zhou, and Mr. Taylor for opening their laboratories, providing testing equipment and support. Much appreciation for Mrs. Wilson and Mr. Mastny from the Illinois Department

## ACKNOWLEDGMENTS (Continued)

of Transportation for their invaluable field expertise and direction during all phases of this research.

## TABLE OF CONTENTS

<u>CHAPTER</u>		<u>PAGE</u>
<b>1</b>	<b>INTRODUCTION . . . . .</b>	<b>1</b>
1.1	Statement of Problem . . . . .	1
1.2	Approach . . . . .	3
1.3	Structure of Thesis . . . . .	4
<b>2</b>	<b>LITERATURE REVIEW . . . . .</b>	<b>5</b>
2.1	Introduction . . . . .	5
2.2	Nonlinear Ultrasonics . . . . .	5
2.3	Ultrasonic Wave Generation in Elastic Medium . . . . .	8
2.4	Stress Identification in Structural Systems . . . . .	12
2.5	The Application of Nonlinear Ultrasonics for Stress Measurement . . . . .	13
<b>3</b>	<b>NUMERICAL STUDIES . . . . .</b>	<b>19</b>
3.1	Method and Equipment . . . . .	19
3.2	Time Domain Models . . . . .	20
3.2.1	Results . . . . .	22
3.3	Frequency Domain Study with Stressed Body . . . . .	24
3.3.1	Results . . . . .	24
<b>4</b>	<b>EXPERIMENTAL STUDIES . . . . .</b>	<b>27</b>
4.1	Equipment . . . . .	27
4.1.1	Ultrasonic Equipment . . . . .	28
4.1.2	Load Testing Equipment . . . . .	31
4.2	Variables Affecting Measurements . . . . .	31
4.2.1	Coupling Effects . . . . .	31
4.2.1.1	Cleaning Excess Couplant . . . . .	32
4.2.1.2	Pulse-Echo Coupling Calibration . . . . .	33
4.2.2	Paint Effects . . . . .	39
4.3	Uni-Axial Load Study . . . . .	42
4.3.1	Small Scale 'L' Shape Test . . . . .	42
4.3.2	Plate Test . . . . .	45
4.3.3	Painted Plate Test . . . . .	48
4.4	Biaxial Load Study . . . . .	51
4.4.1	Painted Plate, Measurement Parallel with Vertical Loading . . . . .	53
4.4.2	Unpainted Plate, Measurement 45 Degree With Vertical Loading . . . . .	56
4.5	Summary . . . . .	59

## TABLE OF CONTENTS (Continued)

<u>CHAPTER</u>		<u>PAGE</u>
<b>5</b>	<b>FIELD DEMONSTRATION</b> . . . . .	61
5.1	Bridge Overview . . . . .	61
5.2	Numerical Gusset Plate Solution . . . . .	62
5.3	Ultrasonic Measurement . . . . .	65
5.4	Ultrasonic Results . . . . .	70
5.5	Summary . . . . .	73
<b>6</b>	<b>CONCLUSION</b> . . . . .	75
6.1	Summary . . . . .	75
6.2	Findings . . . . .	75
6.3	Future Work . . . . .	77
	<b>APPENDICES</b> . . . . .	79
	<b>Appendix A</b> . . . . .	80
	<b>Appendix B</b> . . . . .	82
	<b>CITED LITERATURE</b> . . . . .	85
	<b>VITA</b> . . . . .	88

## LIST OF TABLES

<b><u>TABLE</u></b>		<b><u>PAGE</u></b>
I	Rayleigh Surface Wave Penetration Depth From Contact Surface	10
II	Wave Distortion Stress Correlations From Literature . . . . .	18
III	Hyper-Elastic Murnagham Material Constants . . . . .	20
IV	Effect of Pulse-Echo Coupling Frequency Adjustment . . . . .	38
V	Experimental Stress Comparison with Finite Element Model Results	43
VI	Summary of Uni-Axial Frequency - Stress Correlation Results . .	50
VII	Summary of Frequency - Stress Correlation Results . . . . .	60
VIII	Finite Element Stress Solution to Gusset Plate L10 . . . . .	65
IX	Measured Solution to Gusset Plate L10 . . . . .	73

## LIST OF FIGURES

<u>FIGURE</u>		<u>PAGE</u>
1	Bridge Failures in the United States with Respect to Bridge Type .	2
2	Velocity change due to the stress, (a) longitudinal waves, (b) shear waves . . . . .	8
3	Rayleigh Surface Wave Displacement Mode . . . . .	10
4	Rayleigh Surface Wave In-Plane Displacement Amplitude vs Wavelength ( $\lambda$ ) (Levy, 2001) . . . . .	11
5	Snell's Law Applied to Wave Boundary Interfaces, $l$ Longitudinal Wave, $s$ Shear Wave, $t$ Transverse Wave . . . . .	12
6	A Typical Measurement Approach for Stress Using Nonlinear Acoustics (Rizzo and Lanza di Scalea, 2003) . . . . .	17
7	Time-Domain Thickness Model and Meshing Geometry . . . . .	21
8	Time-Domain Thickness Solution . . . . .	23
9	Frequency-Domain Response 1 MHz Perturbation Numerical Solution	25
10	Numerical Solution Peak Frequency Response Shift vs Applied Stress	26
11	Design Layout of Surface Measurement Technique . . . . .	28
12	Constructed Wedge Separation Handle . . . . .	29
13	Pocket UT System with Transducers and Wedges . . . . .	30
14	Experimental Results from Unloaded Roughness and Coupling Error	33
15	Time Domain Pulse-Echo Coupling Shift Example . . . . .	35
16	Unloaded Ultrasonic Wedge Recoupling Error and Recorded Wedge Pulse-Echo Shifts . . . . .	37
17	Unloaded Ultrasonic Wedge Recoupling Error With Steps for Each Wedge Pulse-Echo Corrections . . . . .	37
18	Laboratory Brush Painted Protective Zinc Based Coating . . . . .	39
19	Unloaded Sample: No Paint vs Paint Frequency and Deviation . . .	40
20	"L" Shape Finite Element Model . . . . .	43
21	Small Scale 'L'-Shape Uni-Axial Stress vs Peak Frequency . . . . .	44
22	0.375 in. (9.2 mm) Thickness A572 Grade 50 Plate Mounted on Uniaxial Load Machine . . . . .	45
23	0.375 in. (9.2 mm) Thick Plate Uniaxial Stress Waveform . . . . .	46
24	0.375 in. (9.2 mm) Thick Plate Uniaxial Stress vs Peak Frequency .	47
25	Painted Time Domain and Frequency Domain Stress Waveform . . .	49
26	Painted Uniaxial Stress vs Peak Frequency . . . . .	49
27	Plate Mounted in Biaxial with Sensor Aligned on Angle . . . . .	52
28	Biaxial Measurement Result Parallel with Vertical Loading Reference	53
29	Biaxial Result Sensor Parallel with Vertical Loading Reference . . .	54
30	Biaxial Result Parallel with Loading Vertical Loading Reference - Horizontal Stress Effect Removed . . . . .	55

## LIST OF FIGURES (Continued)

<u>FIGURE</u>		<u>PAGE</u>
31	Biaxial Result Angled 45 <sup>0</sup> from Loading Reference . . . . .	56
32	Perpendicular Stress Effect Removed Biaxial Result Angled 45 <sup>0</sup> from Loading Reference . . . . .	57
33	SAP2000 Bridge Overview . . . . .	62
34	Side Picture of L10 Gusset Plates Connection . . . . .	63
35	Gusset Plate Numerical Model Stress Solution . . . . .	64
36	Gusset Plate L10 on Field Bridge . . . . .	66
37	Coupled Ultrasonic Wedge Sensor in Positions A, B, C Respectively	67
38	Field Painted, Lab Painted and No Paint on Pulse-Echo Rate of Decay	70
39	Through Transmit, Uncorrected Measurements . . . . .	71
40	Through Transmit, Pulse-Echo Adjusted Measurements . . . . .	72
41	Field Gusset Plate Von Mises Stress (MPa) . . . . .	83
42	Field Gusset Plate Shear Stress (MPa) . . . . .	84

## SUMMARY

A study on the acoustoelastic ultrasonic stress effects in the frequency domain was carried out with a focus on structural steel gusset plates. The primary objective was to construct a field device to provide measuring capabilities for engineers performing structural inspections.

Numerical studies were performed in the time domain and frequency domain to identify critical device design parameters. In the time domain study a minimum wave frequency was determined based on the common gusset plate thicknesses. With a set perturbation frequency, a stressed study was performed in the frequency domain to confirm the expected frequency shift.

A paired wedge device was constructed to easily attach to the surface of an exposed steel member. Upon initial testing ultrasonic coupling and surface repeatability issues were identified. Methods to mitigate the large effects of varying surface coupling conditions were developed and implemented.

The relationships between applied stress and peak perturbation frequency shift were explored. Three critical areas of tests were performed: the uniaxial case, the biaxial parallel loading case and the biaxial angled loading case. Satisfactory linear or bilinear relationships were found for all cases, except the biaxial angled loading case.

A field test was conducted on a fracture critical Pratt Truss bridge gusset plate. The results of the field test when compared with a numerical model confirm the frequency shift with increased loading stress. The accuracy of the field test are affected from suspected shear

## SUMMARY (Continued)

influence factors in the biaxial angled loading case. Further research has been identified to reduce the error to more applicable bounds for inspection duties.

# CHAPTER 1

## INTRODUCTION

### 1.1 Statement of Problem

Wardhana and Hadipriono (Wardhana and Hadipriono, 2003) presented the bridge failures in the United States up to 2000. They reported that 53% of the failures are due to the major flood disasters, 20% of the failures are due to bridge overload and later impact forces from trucks, barges and trains. The remaining 27% of the failures are due to the design, detailing, construction, material and maintenance errors, which may cause unexpected failures. A comprehensive literature survey was conducted and found thirty-four bridge failures between 2000 and 2012. Based on the updated list (Wardhana and Hadipriono, 2003) including failures up to 2012, two bridge types dominate the failures: multi-girder steel bridge and steel truss bridge. Figure 1 shows the pie distribution of failures of different bridge types. Multi-girder bridges and steel truss bridges have the failure percentages of 28% and 22%, respectively. Non-redundant characteristics of these bridge types cause them to be more prone to unexpected failures. These bridges should be closely investigated and their overstressed conditions should be identified in a timely manner in order to prevent such failures.

Increasing demand in transportation and variations in the structure due to renovations may increase the contribution of dead load stress, and as a consequence, unexpected failure. For instance, Liao et al. (Liao et al., 2011) demonstrated that the failed gusset plate of the I-35W



available to measure the actual stress-state of structurally critical bridge components. This is a huge gap in the crucial information of critical elements in non-redundant bridges.

## 1.2 Approach

The proposed concept is to use nonlinear acoustoelastic theory in order to detect the actual load and stress state on selected structural elements. Acoustoelasticity is the dependence of ultrasonic wave speed and polarization on stress. A small ultrasonic perturbation is introduced to the structure through an ultrasonic transducer. The ultrasonic mode used is through transmission. Therefore, the propagating wave is detected by another ultrasonic transducer a set distance away. If the method is routinely used by the bridge inspectors, the change in the portion of the dead load carried by those elements can be identified and used as an indication of damage in other elements. When the structural capacity of a member is reduced due to damage (e.g. crack growth, section loss due to corrosion), load is redistributed. If the structure has redundancy, then the load is redistributed to other members that start to carry higher loads. If the change in live load strain is insignificant due to high dead-load to live-load ratio, conventional strain gauges will not have sufficient sensitivity to identify the load path. When there are over-stressed conditions of the members, they can be identified, and precautions can be taken in a timely manner. The other benefits of measuring the actual stress-state of bridge components are the verification of finite element models and deeper understanding in the uncertainties of structural connection models.

The fundamental challenges of this approach are as follows:

- *Effect of surface texture along the path of ultrasonic measurement:*

Steel members usually have a protective layer on the surface which may not be uniform due to time dependent deterioration. This challenge will be addressed through using localized regions of low stress to generate a baseline measurement to compare against other expected high stress regions.

- *Effect of surface mounting:*

Contact condition can significantly affect the waveform signature and its properties such as frequency content and amplitude. Repeated measurements will be taken to reduce the error and a correction factor will be created using the pulse-echo responses of each transducer.

### **1.3 Structure of Thesis**

The structure of this thesis begins with a background review of relevant acoustoelastic stress wave propagation. Chapter 3 will present numerical studies that confirm thickness tolerance of the method and overall stress-induced frequency shift of the generated waveform. Chapter 4 presents an experimental investigation into the frequency shift experienced in loaded specimens. Specimens presented include biaxial tension loading of unpainted and painted plates, uniaxial tension/compression loading of unpainted and painted plates and uniaxial loading of unpainted "L" profile. The application of the proposed approach in stress measurement of gusset plates at a truss bridge in Chicago is discussed in chapter 5. Finally chapter 6 will provide an overall discussion of the project as a whole, and on future work.

## CHAPTER 2

### LITERATURE REVIEW

#### 2.1 Introduction

This research utilizes the nonlinear dependence of stress and ultrasonic waves in order to identify the stress state of critical bridge structures. In order to provide the theoretical background of the approach, the fundamental theory of nonlinear ultrasonics is described in this chapter. The generation and detection of various wave modes in plate like structures are discussed. Then current approaches to measure stress state of structures are presented. Finally, the applications of nonlinear ultrasonics to identify the stress in the literature are described.

#### 2.2 Nonlinear Ultrasonics

The nonlinearity between the stress and the ultrasonic velocity is driven using the finite deformation theory. In other words, the final coordinates of deformed points are not represented by the original points. Considering the initial state of the deformed body as the independent variable, the wave equation is formulated using the Lagrangian coordinates as,

$$\rho_0 \frac{\partial^2 \mathbf{U}}{\partial t^2} = \nabla_a \cdot \mathbf{P} \quad (2.1)$$

where  $\rho_0$  is the material density,  $\mathbf{U}$  is displacement with respect to original or natural form  $\mathbf{a}$ ,  $\nabla_a$  is the gradient with respect to material coordinates  $\mathbf{a}$ ,  $\mathbf{P}$  is the first Piola-Kirchhoff stress tensor. As an example for purely longitudinal motion (Norris, 1998), the equation becomes

$$\frac{\partial^2 U}{\partial t^2} = c_l^2 \frac{\partial^2 U}{\partial a^2} g \left( \frac{\partial U}{\partial a} \right) \quad (2.2)$$

where  $c_l$  is the longitudinal wave velocity,  $g(\epsilon) = 1 + (3 + c_{111}/(\rho_0 c_l^2))\epsilon + \dots$ ,  $c_{111}$  is the third order elasticity (TOE) constant. The coefficient of nonlinearity for longitudinal wave motion is defined as

$$\beta = -\left(\frac{3}{2} + \frac{c_{111}}{2\rho_0 c_l^2}\right) \quad (2.3)$$

If the source of excitation is  $U(0, t) = U_0 \sin(\omega t)$ , the propagating second harmonic is

$$U(a, \tau) = U_0 \sin(\omega t) + \frac{\beta}{4} \left( \frac{\omega U_0}{c_l} \right) a \cos(2\omega t) \quad (2.4)$$

Measuring the second harmonics for the selected input frequency provides  $\beta$  and consequently TOE  $c_{111}$  using Equation 2.1.

The solution of the eigenvalue problem of Equation 2.1 for plane waves provides the stress-velocity equations for longitudinal  $V_L$  and shear  $V_S$  waves when the stress is generated in the longitudinal direction are given in Hughes (Hughes and Kelly, 1953). With the relevant

equations provided as Equation 2.5 and Equation 2.6,  $\lambda$  and  $\mu$  are Lamé constants,  $l$ ,  $m$  and  $n$  are the third order elasticity constants.

$$\rho_0 * V_L^2 = \lambda + 2\mu + \frac{T}{3K_0} \left[ 2l + \lambda + \frac{\lambda + \mu}{\mu} (4m + 4\lambda + 10\mu) \right] \quad (2.5)$$

$$\rho_0 * V_S^2 = \mu + \frac{T}{3K_0} \left( m + \frac{\lambda n}{4\mu} + 4\lambda + 4\mu \right) \quad (2.6)$$

Using the constants as  $\lambda = 1.5E11$  Pa,  $\mu = 7.5E10$  Pa,  $l = -3E11$  Pa,  $m = -6.2E11$  Pa,  $n = -7.2E11$  Pa and  $\rho = 7850kg/m^3$  for the structural steel, Figure 2 shows the velocity change due to the stress when the acoustoelastic effect is considered. Figure 2a shows the case where the waves propagate in the same direction as the stress. Figure 2b shows the case where the waves are detected in the vertical direction as compared to the stress direction. The velocity change in the longitudinal direction from 0 MPa stress ( $V_L = 6181.954$  m/sec) to 250 MPa stress ( $V_L = 6166.480$  m/sec) is 0.25 %. The velocity change in the vertical direction from 0 MPa stress ( $V_S = 3090.977$  m/sec) to 250 MPa stress ( $V_S = 3090.462$  m/sec) is 0.017 %. The data also shows that the longitudinal direction is more sensitive to the stress when the longitudinal perturbation is introduced. However, the third order elasticity constants may vary due to the variations in the composition of steel.

In summary, the nonlinearity of the stressed body is measured in two parameters:

- The amplitude change of the second order harmonics
- The shift in wave velocity measured in time domain data for amplitude or in frequency domain data for phase

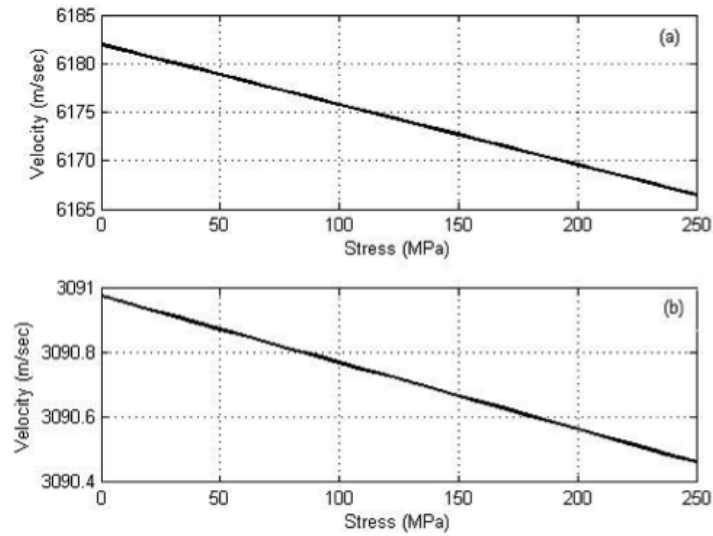


Figure 2. Velocity change due to the stress, (a) longitudinal waves, (b) shear waves

In this study, the stress is measured using the phase shift in the frequency domain as the amplitude of the second harmonics is influenced from the coupling condition more than the wave frequency.

### **2.3 Ultrasonic Wave Generation in Elastic Medium**

The highway bridge components, especially gusset plates, have a typical thickness of 3/8 inch (9.5 mm). Due to the relatively thin cross section, the plate waves dominate the propagating elastic waves. Considering the dispersion curve of a steel plate, wave velocity changes with the plate thickness (Achenbach, 1973) for a particular wave frequency. Therefore, if plate waves are selected to monitor the stress, the baseline wave velocity for the unstressed condition needs

to be measured for each plate thickness. However, the surface waves penetrate only a certain depth of plate.

The Rayleigh wave is a surface wave that is generated out of the combination of the compressive and shear wave. The best way to capture the movement of the Rayleigh wave is to picture the water movement in an ocean wave (ASM Handbook Committee, 1976). The wave energy moves through the water while the individual particles move in an orbital pattern. The ocean waves only affect the top region of the ocean while the lower stretches are untouched. An illustration of this concept is provided in Figure 3. Within the figure, wavelength is presented as  $\lambda$  and the disturbed metal boundary is presented in the shaded region. The orbital displacement oscillation of each surface particle is illustrated on the left side of the figure. The penetration depth is the distance between the at-rest surface and the lowest point of significant particle displacement in the media.

Rayleigh waves penetration depth into a medium is determined by the wavelength. A general plot of the exponential energy decay is provided in Figure 4. For reference, Table I provides practical (90% energy dissipated) Rayleigh wave penetration depths for various frequencies in structural steel (Longitudinal wave speed approx. 5900m/s).

At the boundaries of a body, a transfer of wave energy occurs, in which part is reflected and another part is refracted. Similar to light propagation, the direction and magnitude of each part is determined by following Snell's Law. The magnitude of the reflection is determined by the ratio of the acoustic impedance and the incident angle of transmission. The acoustic impedance ( $Z$ ) is determined by the wave velocity ( $m/s$ ) times the density ( $kg/m^3$ ) resulting

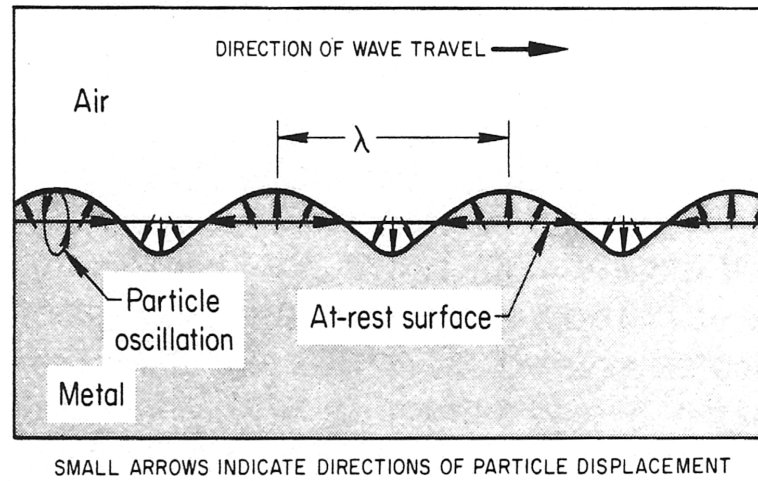


Figure 3. Rayleigh Surface Wave Displacement Mode  
 Reprinted with permission of ASM International.  
 All rights reserved. [www.asminternational.org](http://www.asminternational.org)

TABLE I

Rayleigh Surface Wave Penetration Depth From Contact Surface

Frequency (MHz)	Wavelength (mm / in.)	90% Energy Dissipated Rayleigh Wave Depth (mm / in.)
0.3	19.65 / 0.774	28.44 / 1.161
0.5	11.79 / 0.464	17.07 / 0.697
0.7	08.43 / 0.332	12.20 / 0.498
1.0	05.89 / 0.232	08.53 / 0.348
5.0	01.17 / 0.046	01.72 / 0.070
10.	00.57 / 0.023	00.86 / 0.035

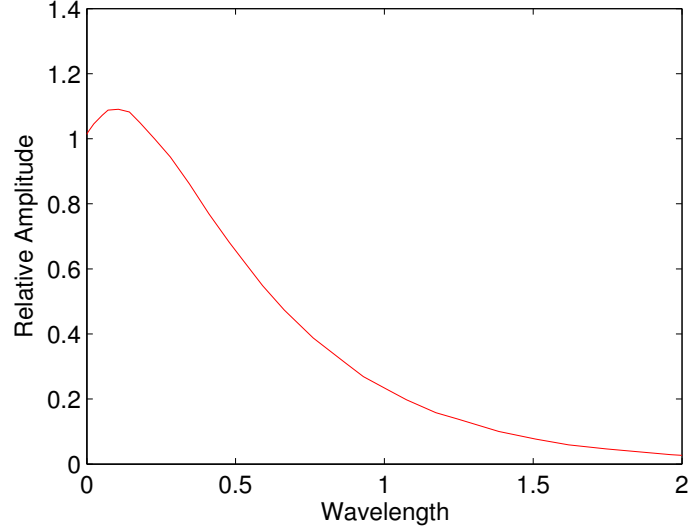


Figure 4. Rayleigh Surface Wave In-Plane Displacement Amplitude vs Wavelength ( $\lambda$ ) (Levy, 2001)

in units ( $g/cm^2$ ). A full table of acoustic properties for various known materials is provided in standard texts (ASM Handbook Committee, 1976). The direction of the refraction or reflection is determined by the incident angle and the velocity of the different bodies. An illustrated example with an introduced longitudinal wave ( $V_l$ ) at incident angle ( $\alpha_l$ ) is provided in Figure 5.

The following equation implements Snell's law relating the resulting wave vectors.

$$\frac{\sin(\alpha_{l(1)})}{V_{l(1)}} = \frac{\sin(\alpha'_{l(1)})}{V_{l(1)}} = \frac{\sin(\beta_l)}{V_l(2)} = \frac{\sin(\beta_t)}{V_t(2)} = \frac{\sin(\beta_s)}{V_s(2)} \quad (2.7)$$

From these equations it is apparent that specific incident angles exist which would cause the exclusion of generation of different wave modes. These unique angles are referred to as the

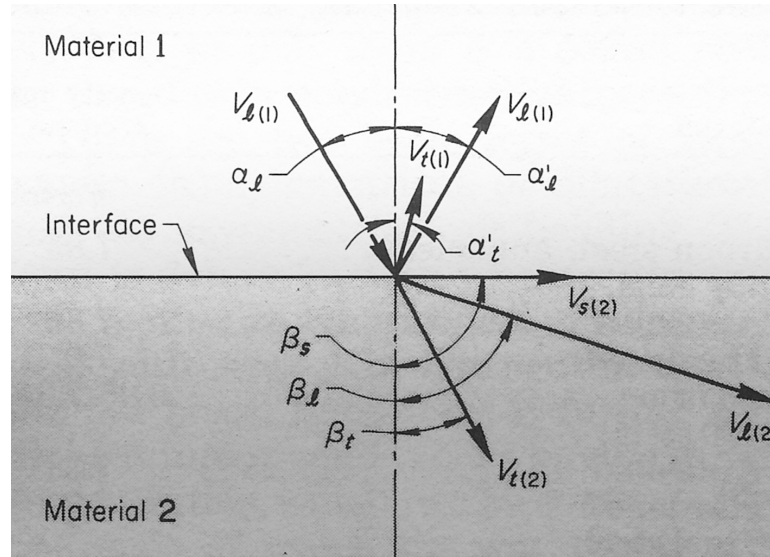


Figure 5. Snell's Law Applied to Wave Boundary Interfaces,  $l$  Longitudinal Wave,  $s$  Shear Wave,  $t$  Transverse Wave

first and second critical angles. At the first critical angle the longitudinal wave refraction angle will equal  $90^\circ$  and subsequently disappear from the medium. The second critical angle will occur when the refraction angle of the transverse wave will equal  $90^\circ$ . When the second critical angle occurs on a relatively traction-free surface, the result is the generation of Rayleigh surface waves.

#### 2.4 Stress Identification in Structural Systems

The existing practiced method for rating and identifying stress deficiencies is through a licensed visual inspection report.

Alternative methods for measuring residual and applied stress are to attach a strain gauge upon construction or after construction. Strain gauges are limited to providing only a change

in strain experienced over the duration of application. The standard for measuring residual uniform stress within a linearly elastic medium is the Hole-Drilling Strain-Gauge Method ASTM E837 (ASTM, 2010).

Gallagher (Gallagher, 2003) researched how ASTM E837 can be applied to steel girder bridges. The method presented in Gallagher (Gallagher, 2003) requires an array of strain gauges and a hole to be drilled into the member. This method has inherent unacceptable risks when performed on a structure or gusset plate with an unknown safety factor.

## **2.5 The Application of Nonlinear Ultrasonics for Stress Measurement**

The use of ultrasonic measurement devices to measure material properties is a well-covered topic. One study by Chaki et al. (Chaki and Bourse, 2009b) is aimed to measure stress levels existing on pre-stress steel tendons. This study was successful in obtaining calibrated measurements of applied stress down to 40% of the ultimate tensile stress. Two critical aspects are apparent in the methods implemented in this study. Firstly, the transducers were placed on the ends of the tendons. The end placement allowed the researchers to apply longitudinal waves (S0 mode). The generation and collection of longitudinal waves is created by a simple perpendicular incident angle. To generate this wave in installed steel components would not be feasible. Secondly, the steel tendon is elongated during applied load testing. This elongation was compensated in the calibration curve for the stress measurement. Since the loading of a bridge component occurs prior to measurement by years, no factor of component deformation is available for consideration.

Junge (Junge, 2003) conducted a similar study of ultrasonic stress measurement. This study focused on the ability of different Rayleigh wave generation methods to measure applied stress. The experimental configuration used both a wedge and a comb method to generate surface waves from a commercial ultrasonic transducer. In the research, the wedge technique of signal generation was determined to be the superior method. The incident angle of the wedge is calculated based of the speed of sound in the wedge material vs. the test object. The surface waves generated with the wedge technique have measured arrivals well separated from sporadic longitudinal and transverse waves. The wave measurement device presented in this paper is a laser doppler vibrometer (LDV). This device allowed the measurement of polarization of the surface-wave to be used as a measurand.

Field use of a LDV measuring device would provide considerable limitations and costs. Since an LDV is a critical component in the applied stress study of Junge (Junge, 2003) further research into methods of stress detection via the wedge technique was sought. Santos et al. (Dos Santos and Bray, 2002) implemented the wedge technique to generate longitudinal waves and measure residual stress in steel members. This study had successful longitudinal wave stress correlation and varying shear wave stress correlations. The use of longitudinal waves for stress detection requires the consideration of thickness of the member being measured. Often with field members thickness is unknown and unseen pitting or defects may make exact thickness measurement a challenging task. The application of surface waves instead of longitudinal waves may allow a more tolerant method stress measurement.

With a focus on surface wave measurement, Egle (Egle and Bray, 1976) presented a surface wave stress identification study. Egle was able to recreate the coefficients presented in Huges (Hughes and Kelly, 1953) and additionally provided error bounds. This research found that rail head treatment and composition do not highly affect the third-order constants. A plot of Rayleigh wave velocity in steel as a rail member is stressed is provided and used as a test confirmation dataset. Also noted in Egle, due to various measuring complications stress correlation details at low stress levels results were inconsistent.

Gokhale (Gokhale, 2007) presented a field measurement of rail stress using an electrical magnetic transducer and an LDV. Due to the availability of automobile-based rail inspection platforms, portability of equipment allowed for heavy ultrasonic equipment to be implemented.

Due to the complex compounding nature of stress loads a bi-axial loaded study is critical to identifying installed stress conditions. Jassby (Jassby and Saltoun, 1981) introduced an initial bi-axial experiment using a disc sample in a uni-axial loading machine. This experiment confirmed the bi-axial linear elastic theory for axially compressed circular plates. Different coefficients of wave distortion were recorded based on the alignment of the applied stress and the position of the measuring device.

Another factor critical to material behavior of in-situ installed steel members is internal member temperature. Zeiger (Zeiger and Jassby, 1982) presented temperature correction coefficients for three variants of steel. For 1080 steel the temperature correction was measured as  $0.63 \text{ ns}/^\circ\text{C}$  per cm of wave path. During the laboratory tests temperature change occurred,

but the magnitude of the temperature correction was within range of the resolution of the measuring device.

A typical ultrasonic configuration used in the literature, Figure 6, requires considering the influence of the extension in the member under loading (i.e. change in distance between transmitter and receiver). This influence effects the arrival time of the wave and it is critical to be identified for determining the wave velocity change with stress. Total time of flight  $t$  corresponding to the total length  $l$  is given as (Chaki and Bourse, 2009b):

$$t = \frac{l_0}{V_0} + \frac{l_\sigma}{V_0(1 + K\sigma)} \quad (2.8)$$

where  $l_0$  is undeformed length,  $V_0$  is unstressed wave velocity,  $l_\sigma$  is the length under stress  $\sigma$ , and  $K$  is nonlinearity factor. The approach requires total deformation of the member measured by strain gauges. The errors in measuring undeformed length  $l_0$  and strain adversely affect the sensitivity of the method. Acoustoelastic calibration curve presented by Chaki and Bourse (Chaki and Bourse, 2009b) shows that the sensor configuration and longitudinal wave mode selected are not sensitive up to 600 MPa.

To summarize the literature correlations, Table II is provided. Each stress acoustoelastic correlation coefficient has been converted into a percent change per unit of stress. Results for aluminum are provided for reference to approximate the effect of material contents. In one study (Berruti, 1996), coupling proved to be a critical factor in the stress correlation regression. General agreement within the steel correlation results for velocity deviation measured parallel

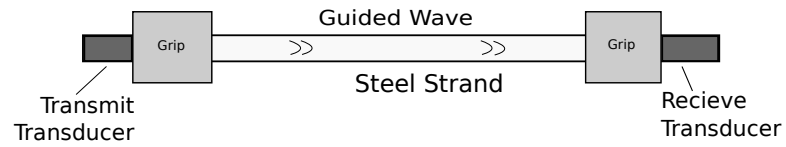


Figure 6. A Typical Measurement Approach for Stress Using Nonlinear Acoustics (Rizzo and Lanza di Scalea, 2003)

with the loading direction provides an average of  $1.17\text{E-}5 \frac{1}{\text{MPa}}$ . The average velocity deviation measured perpendicular with the loading direction was  $4.6\text{E-}6 \frac{1}{\text{MPa}}$ .

TABLE II

Wave Distortion Stress Correlations From Literature

Velocity Test Direction Relation to Loading	Correlation (Abs. % Percent Change/Mpa)	Study Reference
Parallel	1.26E-05	(Egle and Bray, 1976)
Perpendicular	1.25E-06	
Parallel (Aluminum)	1.09E-06	(Jassby and Saltoun, 1981)
Perpendicular (Al.)	7.30E-07	
Parallel	1.25E-05	(Zeiger and Jassby, 1982)
Perpendicular	3.50E-06	
Parallel Recoupling	1.25E-05 / 9.41E-06	(Berruti, 1996)
Parallel	1.01E-05	(Hu et al., 2009)
Perpendicular	9.05E-06	
Parallel 7-Wire Strand	4.78E-04	(Chaki and Bourse, 2009a)

## CHAPTER 3

### NUMERICAL STUDIES

#### 3.1 Method and Equipment

To begin research and application of a non-destructive stress identification device, numerical studies were performed to confirm various critical variables. Finite element based numerical studies allowed exploration of multiple combinations of frequencies and thicknesses decreasing the required overall laboratory testing. The primary studies that were performed were a time-domain analysis of the thickness influence and the frequency-domain analysis of frequency shift in a stressed structure.

The finite element models were constructed and evaluated within the COMSOL Multiphysics software package. Within the COMSOL Multiphysics software, the primary model used was the structural mechanics module. Time domain models were run using an elastic material model. Frequency domain models were run taking advantage of the Hyper-Elastic Murnaghan material model. This model is best suited for acoustoelastic problems.

The finite element modeling of wave propagation requires very fine meshing and time step to prevent the numerical dispersion error (i.e. mesh velocity different from actual velocity). To simplify the problem and reduce the required degrees of freedom, the plate was modeled as 2D plane strain. The maximum mesh size  $l_{max}$  was determined based on the maximum frequency of interest  $f_{max}$  by Equation 3.1 provided by Hill (Hill et al., 2004). Equation 3.2 gives the

TABLE III

Hyper-Elastic Murnaghan Material Constants

Constant	$\lambda$	$\mu$	$l$	$m$	$n$
Value (Pa)	1.5E11	7.5E10	-3E11	-6.2E11	-7.2E11

required time step  $\Delta t_{max}$  for the dynamic integration. The Hyper-Elastic Murnaghan material constants include  $l$ ,  $m$ , and  $n$  were confirmed by Egle (Egle and Bray, 1976) and are provided in Table III together with the Lamé constants.

$$l_{max} = \frac{\lambda_{min}}{20} \quad (3.1)$$

$$\Delta t_{max} = \frac{1}{20f_{max}} \quad (3.2)$$

### 3.2 Time Domain Models

The first study performed was a time domain analysis of a three cycle sine wave pulse excitation occurring at a 1 MHz frequency envelope, Figure 7. The primary objective of this study was to identify the possible waveform distortion that occurs when the Rayleigh wave achieves full penetration depth beyond the depth of the medium. If a specific wavelength requires a minimum thickness to be thickness-independent, then this would provide a lower bound on the frequencies that can be used in the hand held device. The expectation is that the excess energy will reflect off the lower boundary and generate additional plate waves. The

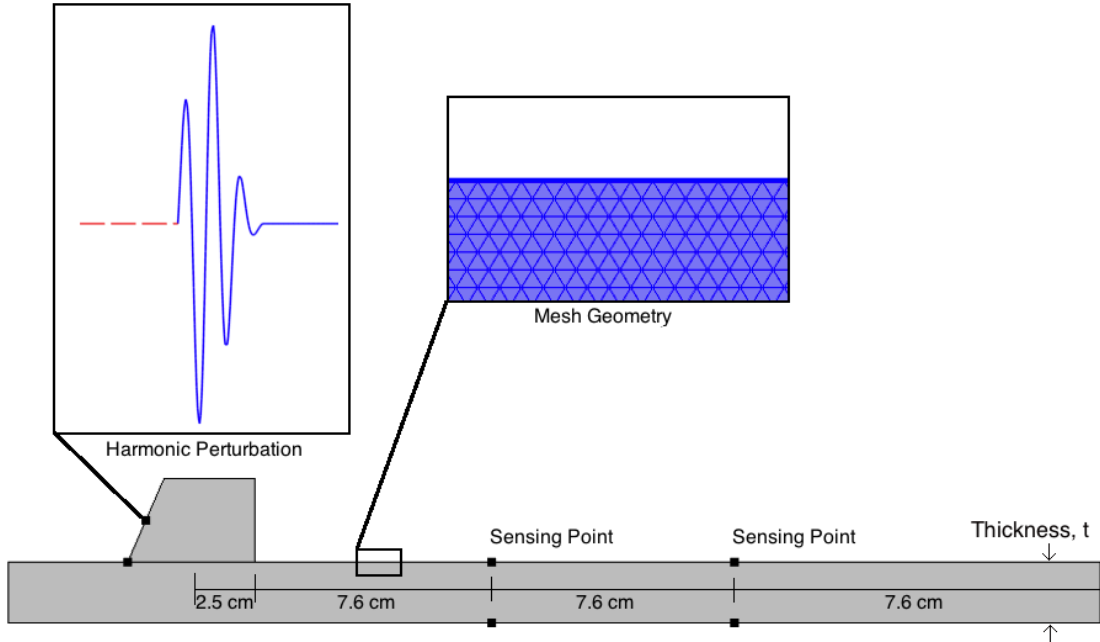


Figure 7. Time-Domain Thickness Model and Meshing Geometry

additional waves will distort the arrival of the Rayleigh wave and render the frequency shift due to stress undeterminable.

The model was generated in the modeling software of COMSOL following the design specifications of a general ultrasonic wedge and plate. Initially, a 1 MHz perturbation was planned to be implemented, although upon meshing of the model it was determined that a 1 MHz perturbation would require computing resources beyond the scope of this investigation. The excitation frequency was adjusted to 700 kHz to reduce the computational intensity. Using Table I, the penetration depth can be referenced depending only on the wavelength. A plot of the harmonic perturbation, geometry and element meshing is provided in Figure 7. The model

thickness was modified and the model re-evaluated for three thicknesses 24.5 mm, 12.3 mm, and 9.2 mm (1.0 in., 0.5 in., 0.375 in.). These three thicknesses cover the base range of standard gusset plates found on existing truss bridges.

### 3.2.1 Results

The horizontal displacement results for each thickness are presented in Figure 8. A general spline interpolation was used to smooth the results of the waveforms. The expected arrival period of the Rayleigh wave was calculated to be approximately 54 *us* at 2800 *m/s* which generally agrees with the time domain solution. A zoom referenced plot is also provided to focus on the Rayleigh arrival period. For reference the penetration depth provided in Table I for a 700 kHz Rayleigh wave is approximately 12mm (0.49 in.).

From the results of the simulation a shift is seen in the arrival period and localized frequency for the 9.2 mm (0.375 in.) model. The 12.3 mm (0.5 in.) and 24.5 mm (1.0 in.) models appear to match with regard to arrival time and localized frequency. These results confirm with the expected results in simplified Rayleigh wave theory. Specifically this study was successful in confirming that above a wavelength determined threshold, thickness is not a factor in waveform arrival. Provided that typical gusset plates installed locally are approximately 9.2 mm (0.375 in.) then the lowest frequency that can be easily applied in a handheld detection device is approximately 1 MHz.

One additional observation that is critical is the observed noise prior to the arrival of the Rayleigh waves in the region of 35-55*us*. This noise is the largest for the smaller thickness and varies non-uniformly with the thicker sections. This noise may be caused by unintended plate

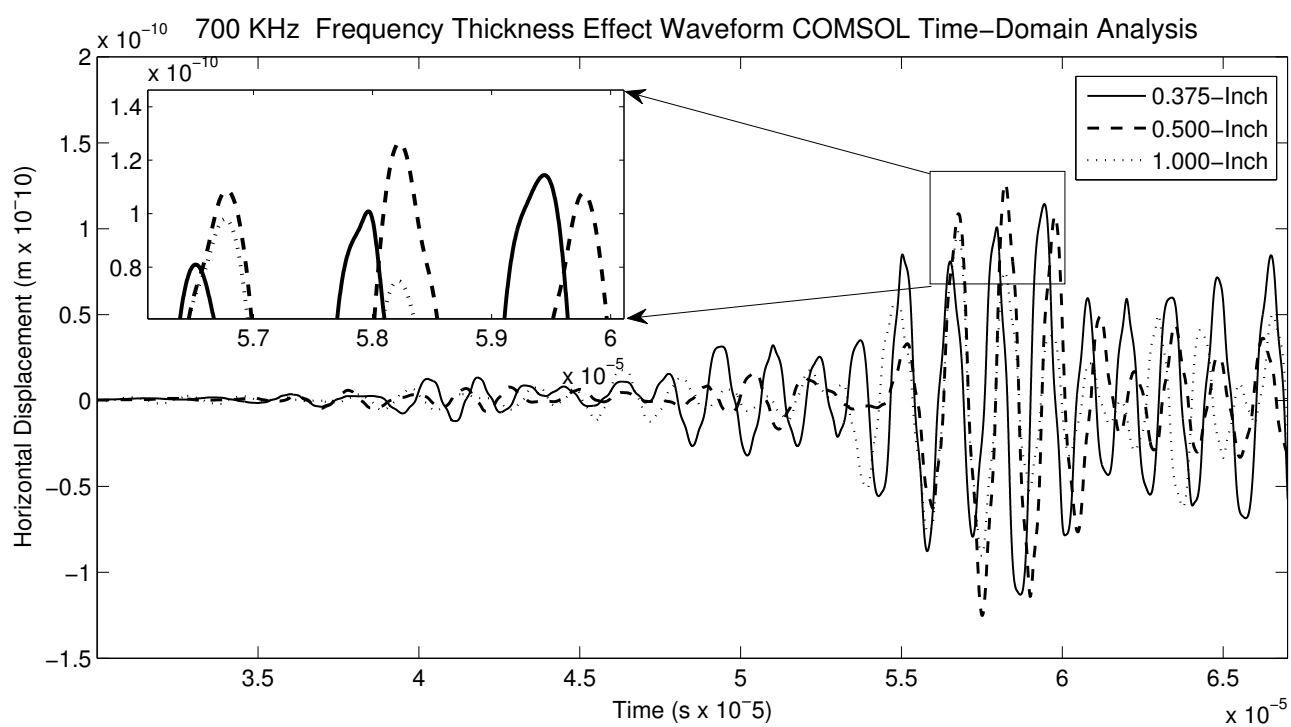


Figure 8. Time-Domain Thickness Solution

waves induced by a small variation of the critical angle. These erroneous waves will have to be monitored and minimized in experimental testing to avoid unnecessary error in measurements by changing the wedge angle.

### **3.3 Frequency Domain Study with Stressed Body**

The second numerical study was a frequency domain study of a stressed medium. This model was constructed using a two stage solution configuration. Firstly, a stationary stage was constructed with the applied prestress on the medium. Secondly, a frequency perturbation stage was calculated over the critical range of frequencies near the perturbation frequency. Finally, the study was repeated for a range of stress states that are within operating range of steel medium. The purpose of this study was to numerically determine frequency shift experienced per unit of stress carried in the steel plate medium.

The numerical model for the frequency domain perturbation calculation was constructed based on the model for the thickness time-domain study. The wedge was removed and replaced with a direct point load perturbation parallel to the plate. This simplification ensured the waveform was not distorted in the wedge and decreased the number of degrees of freedom being solved. Additionally, the frequency domain solution is accurate in simple structural problems (Peng et al., 2009). This model used the Hyper-Elastic Murnagham model with the provided constants.

#### **3.3.1 Results**

The numerical simulation of the frequency-domain response was performed and the results are presented in Figure 9 and Figure 10. Figure 9 provides the frequency-domain amplitude

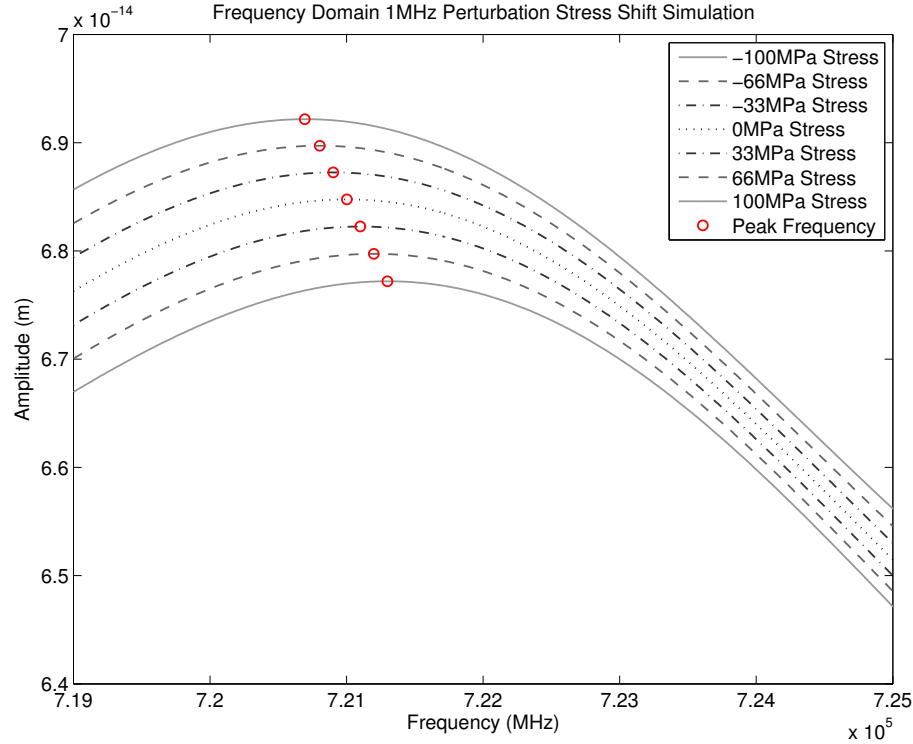


Figure 9. Frequency-Domain Response 1 MHz Perturbation Numerical Solution

response due to a initial perturbation of 1 MHz. The medium initial stress value was then increased and the results were plotted on the same plot. The generated perturbation frequency is 1 MHz while the results provide a distinct peak around approximately 700 KHz. The peak shift may be due to the transfer function present in the media.

Figure 10 provides a simplified presentation of the shift in peak frequency as stress is applied to the medium. The peak frequency shift is quantified in fractional or deviation shift from a zero stress state. The linear slope for the percent shift in peak frequency as a function of stress deviating from zero is  $-4.183\text{E-}12$  % Hz shift / Pa.

The purpose of the hyper-elastic numerical model was to determine the frequency shift experienced as a steel medium was stressed. The results provided a linear shift in peak frequency

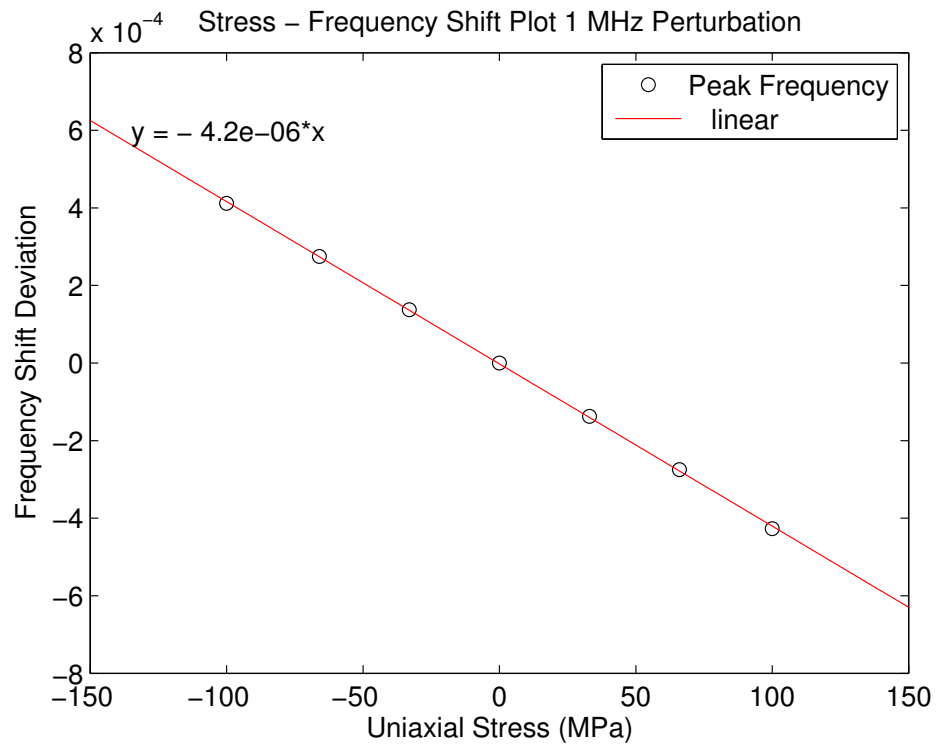


Figure 10. Numerical Solution Peak Frequency Response Shift vs Applied Stress

as the medium was exposed to stressing forces. The magnitude of the shift is small compared to the initial frequency. Converting the presented percent shift into hertz shift provides 3.02 Hz / MPa. This small range of frequency shift provides basis to move forward with the experimental tests.

## CHAPTER 4

### EXPERIMENTAL STUDIES

The laboratory scale experiments performed provide a practical application basis to build understanding of the surface wave acquisition resolution and stress detection practicality. Sensor layout designs and applicable loading fixtures were built to best accomplish ultrasonic testing in a stress steel medium. The three major laboratory goals were to identify repeatability factors, measure uni-axial frequency stress correlation and measure bi-axial frequency stress correlation.

#### 4.1 Equipment

One of the critical constraints on equipment selection for this project was limiting the size and complexity to valid field deployable equipment. This requirement limited the magnitude of viable ultrasonic equipment and surface preparation. To allow the device to be easily attachable to structures free surfaces we will implement a method that can be attached during any stage of a structure's lifecycle. This will remove the need to adjust measurements for media elongation as covered in Equation 2.8. A design layout of the measurement method is presented in Figure 11.

The general method of measurement will be to generate a sinusoidal 1 MHz perturbation to the stressed structure through a piezoelectric ultrasonic transducer. The wedge is positioned at the second critical angle to initiate Rayleigh surface waves. As the wave propagates into the stressed steel the wave distortion will occur adjusting the velocity and ultimately the frequency. The receiving ultrasonic transducer at the other end of the holder, Figure 11, converts

the Rayleigh wave back to electrical output. Using a windowed FFT over the distinct Rayleigh arrival window, the frequency shift will be measured and correlated to a stress value. The ultrasonic transducers are coupled to the structure using ultrasonic gel which allows free movement of the transducers when the structure is stressed. Therefore, the distance between the transmitter and receiver,  $L_o$ , stays constant when the structure extends under stress, Figure 11.

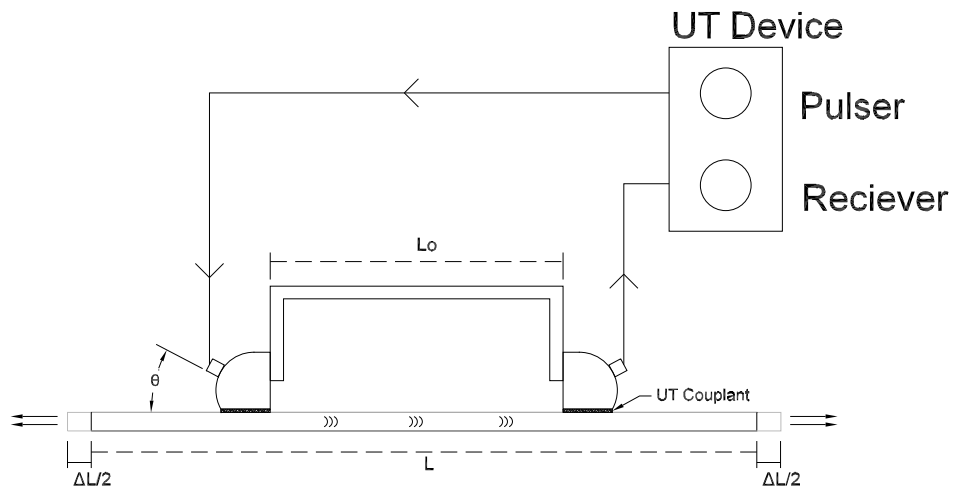


Figure 11. Design Layout of Surface Measurement Technique

#### 4.1.1 Ultrasonic Equipment

The primary testing equipment is a Pocket UT device (Figure 13) manufactured by Mistras Group. This device is a combination of a AD-IPR-1210 Digital to Analog Oscilloscope and a

0-400 Volt variable signal generator. The Pocket UT provides a digital screen waveform readout and comma-delimited file storage for later processing with custom MATLAB processing scripts. The Pocket UT was selected as the ideal device for this project primarily because of the small size and 4 hour battery life.



Figure 12. Constructed Wedge Separation Handle

The wedges selected for Rayleigh wave generation are variable angle beam wedges constructed by Olympus Inspection & Measurement Systems. The transducers used were Panametrics A401S and were selected from Olympus to match the variable angle beam wedges. The supplied and verified longitudinal wave velocity of the wedge was 2720 m/s. The measured wave velocity of the A572 Grade 50 steel was found via pulse-echo technique to be approximately 5950 m/s. The required second critical angle was calculated to be approximately  $62.7^{\circ}$ . The wedges were adjusted to this incident angle and secured for the duration of testing. A handle was

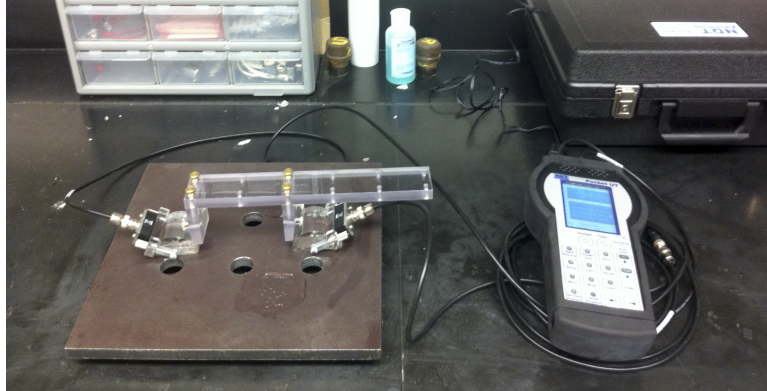


Figure 13. Pocket UT System with Transducers and Wedges

constructed to position the wedges apart at a constant distance and surface orientation. The handle was constructed out of plexiglass to prevent any ultrasonic wave leakage from distorting the Rayleigh arrival. The handle is captured in Figure 13 and detailed in Figure 12.

Transducers were acquired to match the desired transmission frequency of the surface wave. Based on the data presented in Figure 4, the wavelength of the surface wave is a large factor on the penetration depth of the sample. If a Rayleigh wave over penetrates and disturbs the inner boundary of the steel there is a potential for erroneous plate waves to be created. Alternatively, it is important to allow the wave to penetrate deeply into the steel medium to possibly reduce any unpredictable small surface conditions. Table I presents a list of general ultrasonic frequencies and the expected Rayleigh wave penetration depth for 90% of the energy.

Based on discussions with various state department of transportations, the most common gusset plate depth expected will be 0.375 in. (9.2 mm) thick. To optimize penetration while

minimizing the potential to over penetrate a general ultrasonic frequency of 1 MHz was selected to be the ideal frequency. The penetration of a 1 MHz wave in A572 Grade 50 steel with a longitudinal velocity of 5970m/s is approximately 0.35 in. (8.6 mm).

#### **4.1.2 Load Testing Equipment**

Three Instron hydraulic load machines were utilized for the tensile and compression loading of steel samples. The first uni-axial loading machine was used to test small scale L-shaped test sample up to 25 KN of applied load. The second uni-axial loading machine was used to test a full scale plate in a uni-axial loading situation. The second uni-axial machine configuration was capable to apply 115 KN load. The third load machine was a bi-axial load machine capable of applying four loads of 0-20 KN magnitude in perpendicular directions.

#### **4.2 Variables Affecting Measurements**

The first area of focus in experimental studies was identifying factors that were not represented in the numerical studies. The two critical factors that were identified to require additional testing were the coupling condition and the surface paint condition. Efforts were made to quantify the effect of each condition on the repeatability and measurement of the peak perturbation frequency.

##### **4.2.1 Coupling Effects**

Coupling of the ultrasonic system to the steel media is a critical component in the sensitive system. The thickness, viscosity and chemical properties of the coupling method all affect the properties of the waveform that is transmitted and received in the media. The importance of

coupling procedure and method were discovered through trial and error during the early stages of testing.

#### **4.2.1.1 Cleaning Excess Couplant**

To measure the effect of coupling fluid two distinct methods were localized and performed with repeatability. The first method was to apply a dime diameter of coupling fluid on the wedge, then attach and remove without wiping excess coupling fluid (Not Cleaned). The second method was to wipe the excess coupling fluid off (Cleaned) in-between attaching the sensor wedges. The results were also performed for both a hot-rolled (Rough) sample and a machine-ground (Smooth) sample. The addition of this blocked variable was to rule out potential surface influence and provide an additional data set for the coupling effect. The results of 10 coupling repetitions are presented in Figure 14.

Figure 14 provides a box plot with compressed outliers for the Not Cleaned sample sets. The Not Cleaned samples of Rough and Smooth surfaces have a standard deviation of 0.161 MHz and 0.157 MHz, respectively. While the Cleaned samples have a standard deviation of 0.001 MHz and 0.002 MHz. This provides a reduction factor of 100 in range of recorded peak perturbation frequency. Some potential causes may be that the excess couplant dampens the surface or by wiping the surface to remove excess couplant a relatively smoother surface results. From these results all following tests were performed using the cleaned coupling method. The results presented do not show a consistent distinct trend for the effect of roughness on peak frequency measurement. A roughness effect on wave arrival time is reported by Hu (Hu et al.,

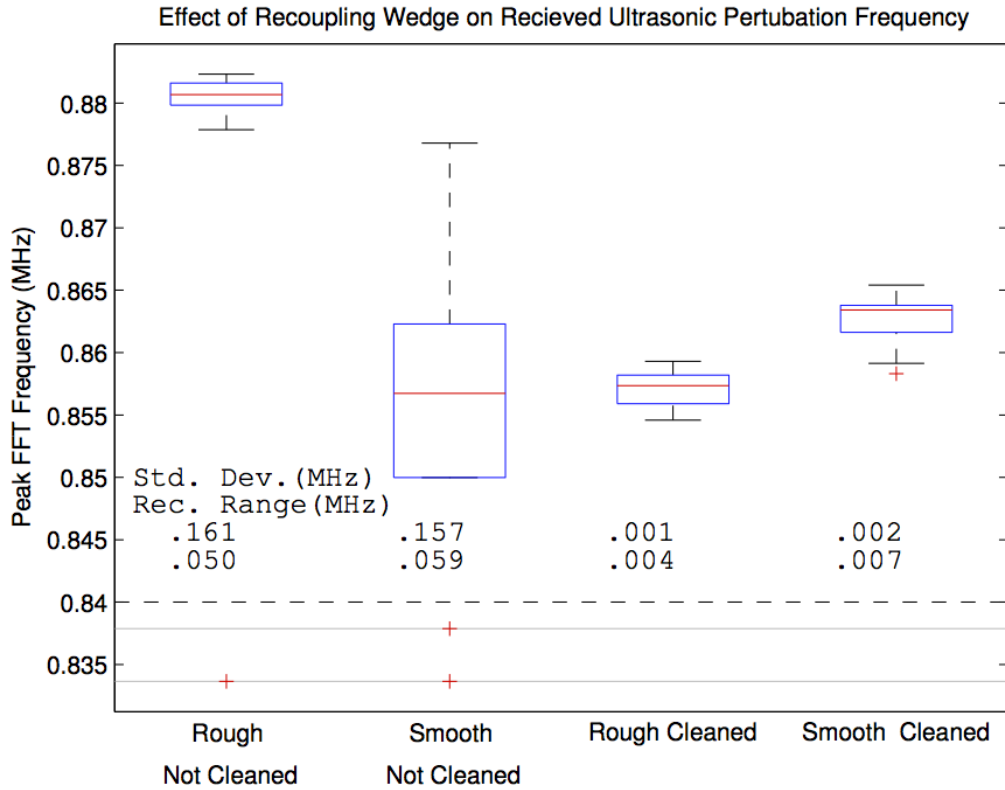


Figure 14. Experimental Results from Unloaded Roughness and Coupling Error

2009) based on the residual error of wave velocity measurements. The resolution and errors in this test did not provide consistent results to confirm the findings.

#### **4.2.1.2 Pulse-Echo Coupling Calibration**

During initial application of the surface wave generation the variation of the waveform due to coupling was greater than the variation due to stress. The need to decrease the variation

due to coupling was investigated. Additional literature by Sun (Sun et al., 2006) was explored and applications to the frequency attenuation were researched. Initial partial implementations of the modified acoustic nonlinearity measurement method produced tests that found a tone-burst was resilient to coupling. Upon further investigation into using a tone-burst waveform, it was observed that the tone-burst waveform was also resilient to stress shift. Unfortunately the decreased response to stress limited the ability to apply harmonic principals as a method of coupling error reduction. Building on the principals of coupling error being due to each wedge, a method of quantifying each wedge's contribution to the error was required.

Upon further investigation it was found that by generating a pulse-echo measurement for each wedge, a waveform region around 40us distorted upon each recoupling. The wave distortion due to the coupling effect is presented in Figure 15. The windowed fast Fourier transform peak frequency on the uncoupled wedges is used as a reference baseline measurement. After each subsequent recoupling, a pulse-echo measurement is generated for each wedge and differenced against the baseline measurement respectively.

The deviation of each wedge as recoupling occurred was visually correlated with the estimated error of the measurement. The two new sets of pulse-echo frequency are applied as a linear filter to the through transit peak frequency measurements. The implementation of this effect is presented in Equation 4.1. Through the use of symmetry or constant loading of the material keeping  $p$  constant, the coupling effect can be reduced. With values obtained for the coupling effect, the remaining measured variable is the material stress response.

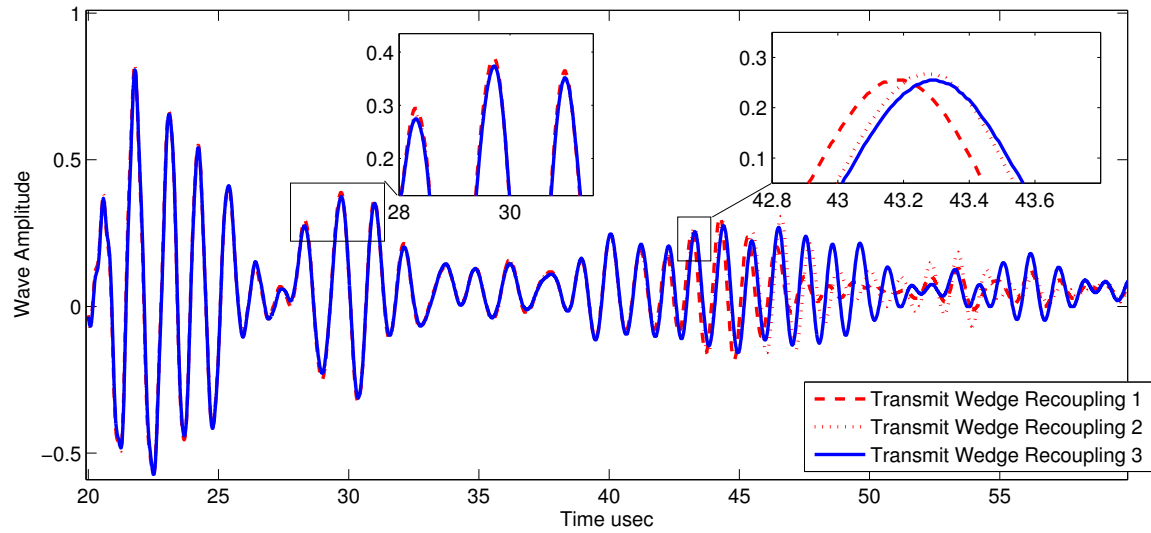


Figure 15. Time Domain Pulse-Echo Coupling Shift Example

$$\text{Measure Frequency} = I * C_T * p * C_R * O \quad (4.1)$$

- |             |  |
|-------------|--|
| $I$         | Input Characteristics of Transmitter Transducer (Constant During Trials) |
| $C_T / C_R$ | The Wedge Coupling Effect  |
| $p$         | The Material Stress Response   |
| $O$         | Output Characteristics of Receiver Transducer (Constant During Trials)   |

The pulse-echo method of measurement for each wedge was then performed for a series of 7 repetitions. Since the contribution of frequency deviation in each wedge is only a percentage of the total error experienced in the through transmission, a factor of contribution is needed. To determine the optimum contribution factor at least two identically stressed regions need to be measured to cancel out the material response ( $p$ ) term of Equation 4.1. With the two or more sets of Equation 4.1 the contribution factor is solved for to reduce the total remaining error. With the best fit contribution factor the effect of coupling is removed from all of the through transmission measurements and the resulting shift due to the material response ( $p$ ) is identified. The measured frequencies are plotted as measured Figure 16. The original transmission and the corrected through transmission shift for each wedge's pulse-echo measurement is presented in Figure 17. The tabulated effect of the pulse-echo adjustment on the standard deviation of the repetitions is found in Table IV.

From the results in Figure 16, the deviation in the through transit frequency are inverse of the deviation in the transmit wedge pulse-echo. Through the proper optimization factor the deviations cancel out to decrease the overall deviation of the measurement. The results presented in Figure 17 show a strong decrease in variation towards a consistent measured frequency for the single stress state. The first measurement in the series experiences the largest error, it is suggestive that this measurement represents the additional human error of initial setup/connections of the system. In Table IV after applying the optimized factors for both additional pulse-echo measurements the overall frequency deviation is reduced by 35%.

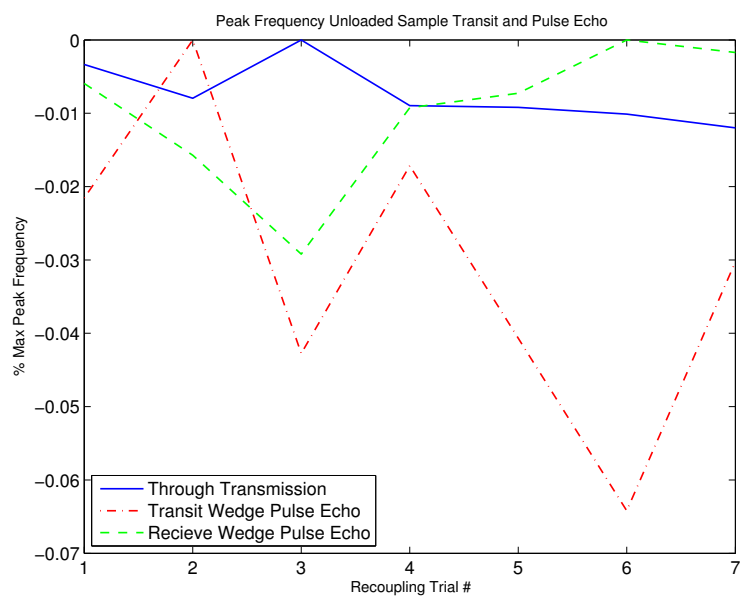


Figure 16. Unloaded Ultrasonic Wedge Recoupling Error and Recorded Wedge Pulse-Echo Shifts

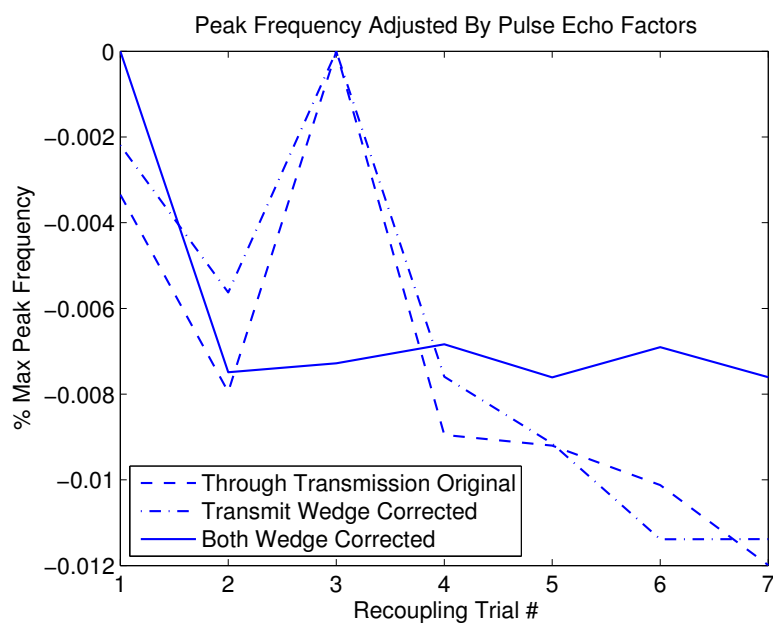


Figure 17. Unloaded Ultrasonic Wedge Recoupling Error With Steps for Each Wedge Pulse-Echo Corrections

TABLE IV

Effect of Pulse-Echo Coupling Frequency Adjustment

	Original	Transmitter Wedge Adjusted	Receive Wedge Adjusted
Std. Deviation (MHz)	3.6E-3	3.7E-3	2.3E-3
Percent Deviation Decrease (%)		-4.5	35.4

#### 4.2.2 Paint Effects

The second important factor on repeatability is surface conditions. Regions of measurement are limited to consistently smooth sections that are able to maintain uniform wedge coupling. The primary unpredictable field variable is the paint thickness. Steel truss bridges are coated with a standard corrosion protective zinc based primer followed by a urethane top coating. To determine the magnitude of the paint effect a 0.375 in. (9.2 mm) sample was painted following the Illinois Department of Transportation Bridge Paint Specification (GBSP 25).

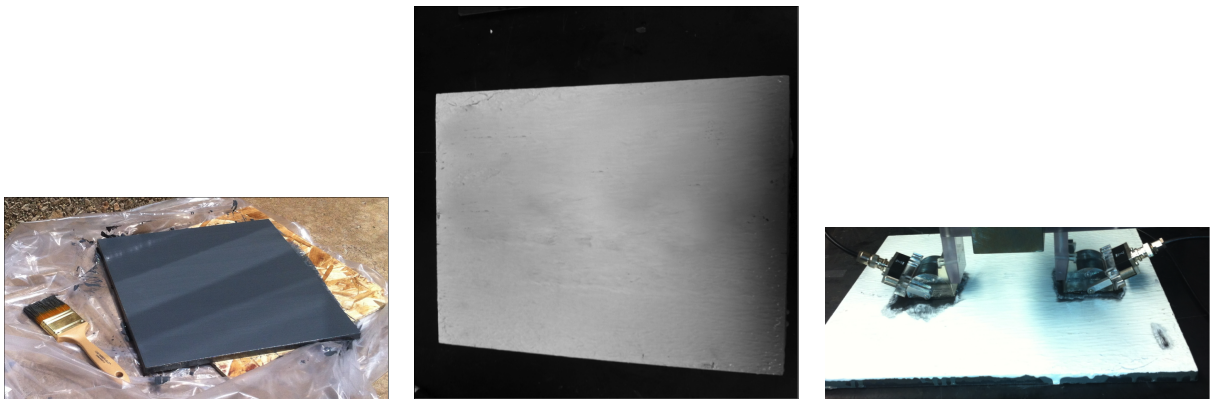


Figure 18. Laboratory Brush Painted Protective Zinc Based Coating  
A) Grey Zinc Primer Applied 1st Coat B) White Fast Clad Urethane Applied 2nd Coat C)  
Wire brushed paint sample

A test was performed recoupling the handheld wedge and measuring the peak frequency and deviation for a group of 10 recouplings at each stage. Three stages of paint conditioning were evaluated as captured in Figure 18. The first stage was an unpainted hot-rolled sample. The second stage was a fully painted sample. The third stage was a painted sample with the wedge coupling area ground clean with a wire brush. Figure 19 presents the results of the tests.

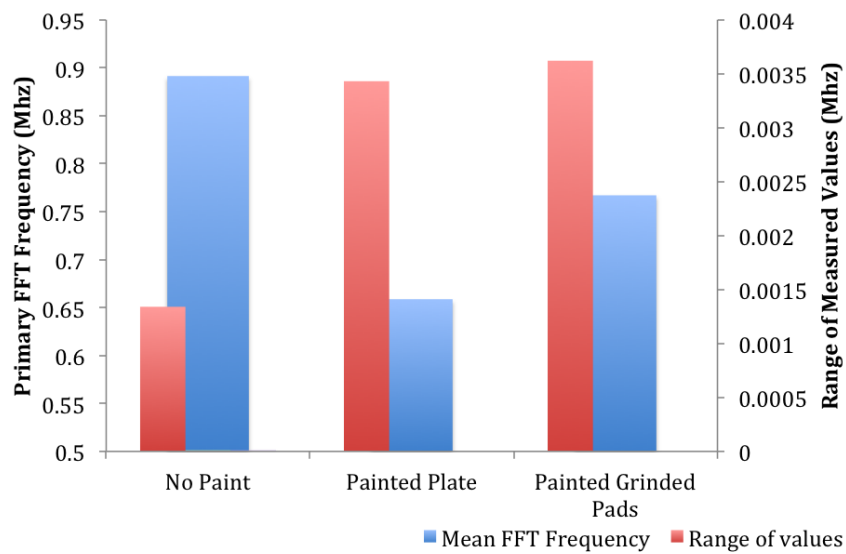


Figure 19. Unloaded Sample: No Paint vs Paint Frequency and Deviation

The peak frequency with no pulse-echo correction for the painted sample was 0.66 MHz, while the unpainted sample was 0.89 MHz. This distinct shift was accompanied by an increase

in standard deviation. The grinded coupling area measured a peak frequency of 0.76 MHz, but no decrease in experienced deviation.

The results of the paint trial confirm the hypothesis that the painted condition plays an important role on the properties of repeatability in peak frequency identification. Method of stress identification will need to compensate for the unique paint effect of each steel installation. The painted surface recoupling test highlights the need to generate an understanding of the painted sample difference in frequency shift due to stress.

### **4.3 Uni-Axial Load Study**

With the repeatability errors identified the next feature to investigate was the stress frequency shift measurand. The first purpose of these tests is to confirm the frequency stress relationship calculated in the numerical studies. The second purpose is to compare the frequency results against the published velocity results.

#### **4.3.1 Small Scale 'L' Shape Test**

The first stressed test was designed for a Uni-Axial applied load. The first test consisted of a 2x2x1/8 A572 Grade 50 "L" shape with strain gauge, stressed in the 25 KN Uniaxial Instron Hydraulic Loading Machine. The small scale test was designed to allow initial testing of device parameters, and coupling behavior prior to designing a full scale testing apparatus.

The method of testing started with the wedge handle coupled at zero stress and then the load was stepped increased. In-between load steps the wedge was not recoupled in order to reduce measurement error at each step. Due to the complex shape a finite element model was constructed to confirm stress distributions recorded by the strain gauge. The finite element model is presented in Figure 20. The finite model confirmed that distribution was constant along the loading direction. At each load step a Rayleigh wave arrival was recorded in the time-domain and converted to the frequency domain within Matlab. To provide a common linear rate of stress influence on peak frequency, the peak frequency results are plotted against applied stress in Figure 21. Multiple tests were run but results were highly influenced by coupling parameters only reproducible results are provided. Variability is suspected to be a factor of the spurious waves generated from full wave penetration.

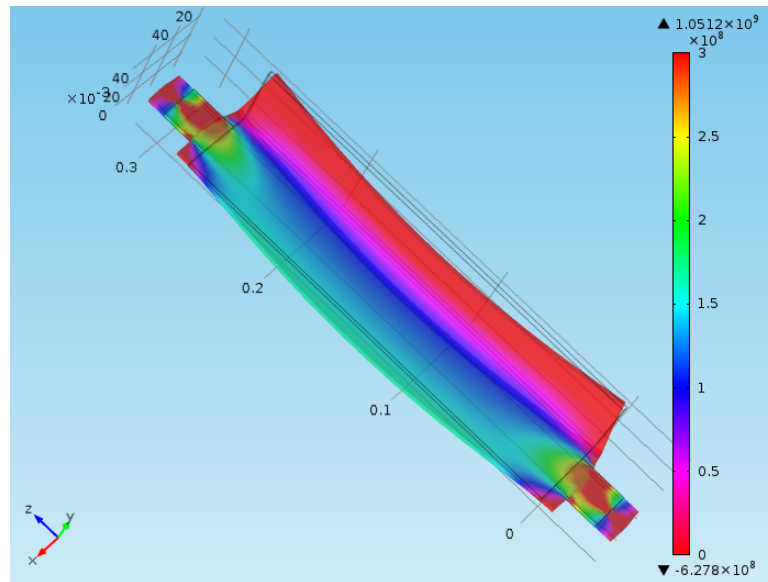


Figure 20. "L" Shape Finite Element Model  
Normal Stress  $\sigma_{zz}$   $N/m^2$ , 25 KN Loading Stage

TABLE V

Experimental Stress Comparison with Finite Element Model Results

Applied Load KN	Finite $\sigma_{zz}$ MPa	Experiment Strain Gauge $\sigma_{zz}$ MPa	% Difference
0	0	0	0.0
5	25.7	25.6	0.4
10	51.4	51.8	-0.7

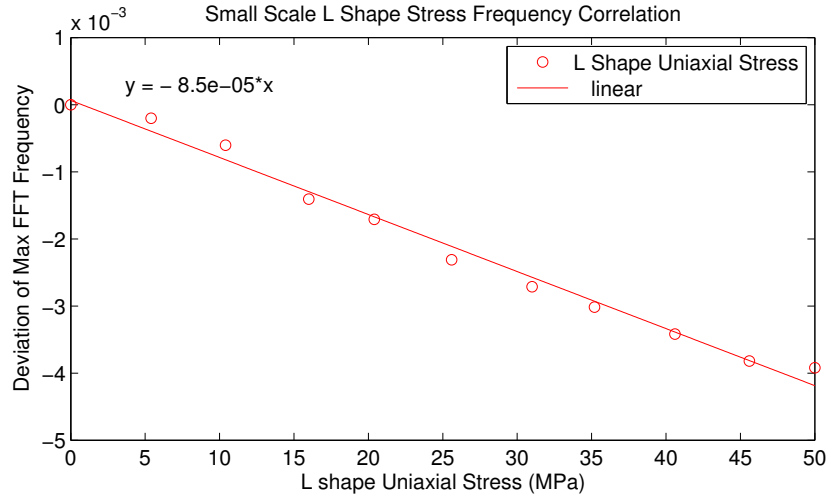


Figure 21. Small Scale 'L'-Shape Uni-Axial Stress vs Peak Frequency

The results of the finite element modeling of the expected stress component in the "L" Shape are compared to the the attached strain gauge in Table V. The observed verse calculated difference was less than 1 percent. This agreement between the two was within range of acceptable laboratory measurements. Further testing will only depend upon the attached strain gauges for measurement of applied stress.

The results of the frequency shift maintain a positive correlation with stress. The decreasing frequency as stress increases agrees with the previous numerical study of the frequency-domain solution. The slope of the linear regression is  $-8.5E-5 \frac{1}{MPa}$ . This is approximately 7 times larger than the average literature percent of change per unit of stress.

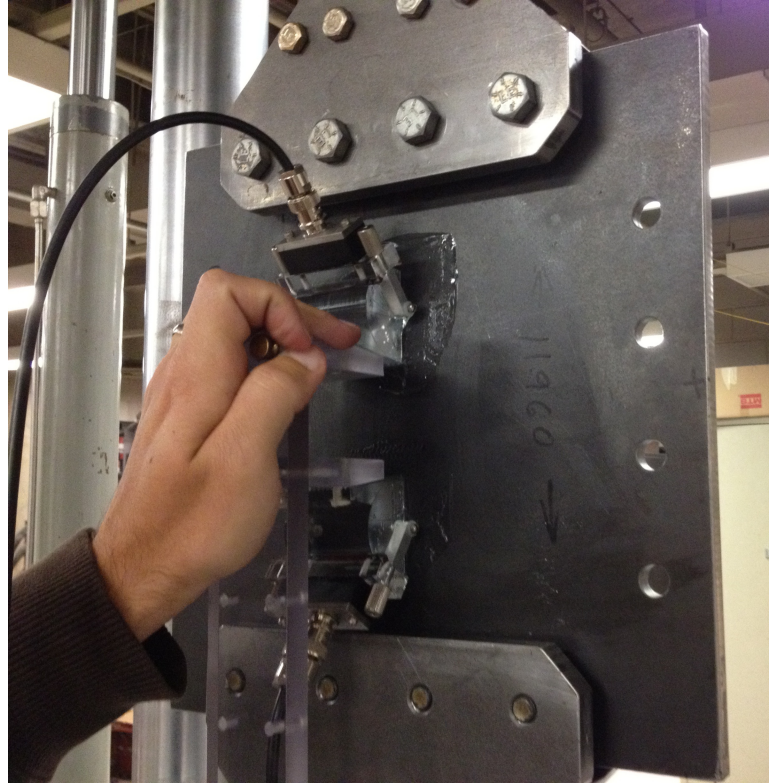


Figure 22. 0.375 in. (9.2 mm) Thickness A572 Grade 50 Plate Mounted on Uniaxial Load Machine

#### 4.3.2 Plate Test

The next uniaxial test setup was designed to test a full size gusset plate thickness. A 12x12x3/8 A572 Grade 50 plate was drilled and mounted in the larger uniaxial Instron hydraulic load machine. A figure of the mounting configuration is provided in Figure 22. The handheld unit was coupled to the plate using a pair of clamps and remained attached for the entire test.

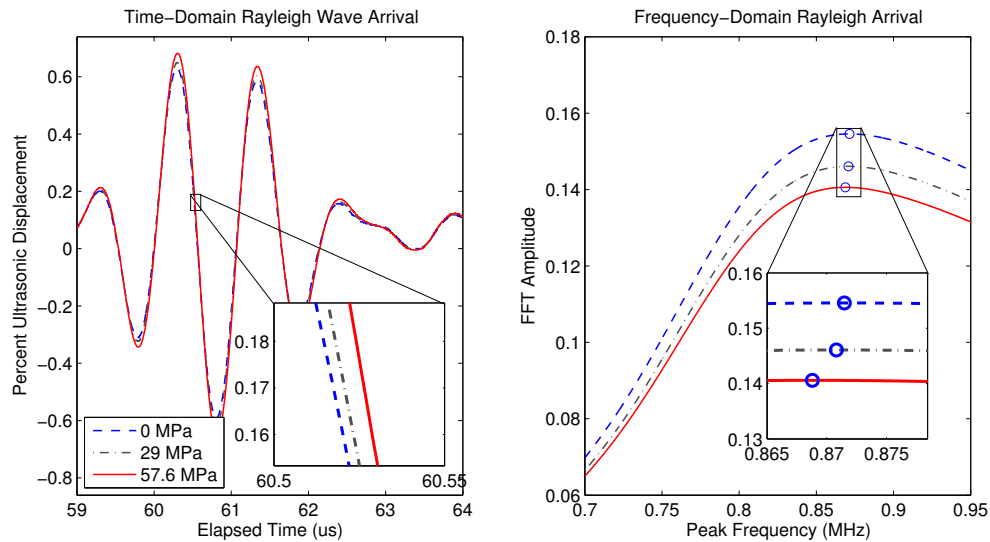


Figure 23. 0.375 in. (9.2 mm) Thick Plate Uniaxial Stress Waveform

The method of testing started with a zero stress waveform measurement with less than 1 KN of loading. The load was increased by 13 KN and a set of three waveforms were recorded per increment up to 110 KN. At the completion of tensile loading a compression loading cycle was performed using increments of 18 KN. Once all of the measured waveforms were collected, post-processing was performed using Matlab. The results of the 0.375 in. (9.2 mm) thick plate for the three stress cases are presented in the time domain in Figure 23. The resulting measured peak frequency plotted against uniaxial stress is presented in Figure 24.

The 0.375 in. (9.2 mm) thick plate frequency stress correlation trends in a linear relationship. The slope of the linear regression is  $-5.4E-5 \frac{1}{MPa}$ . The results for the 0.375 in. (9.2 mm) thick

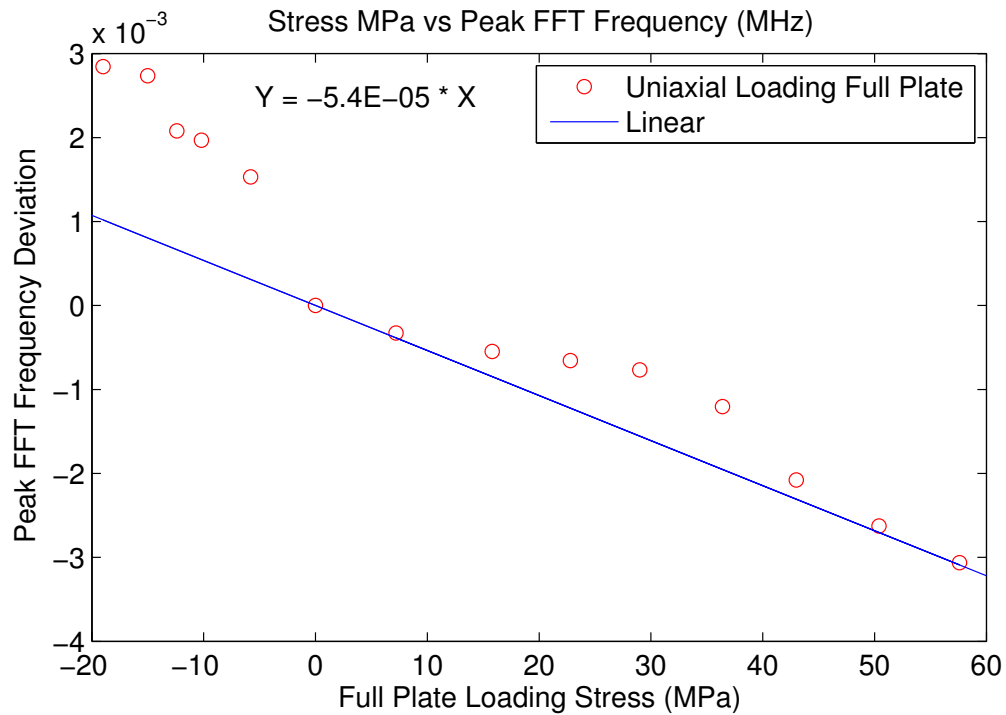


Figure 24. 0.375 in. (9.2 mm) Thick Plate Uniaxial Stress vs Peak Frequency

plate are 36% smaller than the results obtained for the 0.125 in. 'L' shape. This difference between the two may be due to the erroneous peak frequencies captured in the low stress region of the plot. The loading response appears to maintain a consistent slope within the compression and tension regions. The deviation as the stress approaches zero is captured. This deviation suggests additional factors play a role in the acoustical elastic response in low stress regions.

### 4.3.3 Painted Plate Test

The final uniaxial test performed was the painted 0.375 in. (9.2 mm) thick plate. The plate was prepared following the Illinois Department of Transportation Bridge Paint Specification (GBSP 25). The primer and top coat that were used were Sherwin Williams Corothane I Galvapac 1K Zinc Primer(B65G11) and Fast Clad Urethane. Samples were painted using a brush technique and no thinning agent was added to the product. Figure 18 provides visual references for each step in the preparation.

The loading stage of the painted plate test was performed in an identical method to the loading stages of the unpainted plate. A small holding load was applied for a zero load point measurement. Then the tension load was step increased and waveforms were captured at each loading step. The waveforms were processed using Matlab to generate a peak windowed frequency. An example plot of the time domain captured waveform for three stress cases is provided in Figure 25. The plot of the processed frequency domain peak frequency stress correlation is in Figure 26.

The painted uniaxial stress frequency relationship is  $-8.7E-6 \frac{1}{MPa}$ . The results of the stress painted plate agree with the decreased unloaded peak frequency results of the unloaded painted testing. Painting the sample also decreased the magnitude of the stress effect on peak frequency. Visually comparing the results from the unpainted tests, the painting application also increased the residuals present from the linear regression. One factor that may have attributed to the increased residuals is the non-uniform nature of using a brush as the paint applicator. The

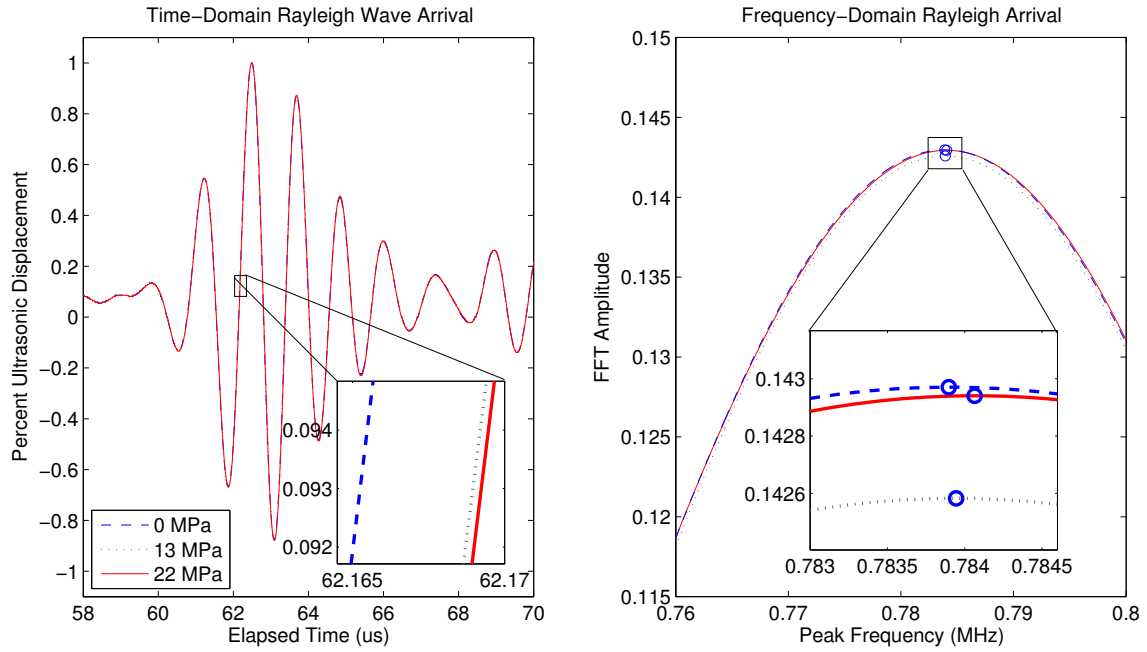


Figure 25. Painted Time Domain and Frequency Domain Stress Waveform

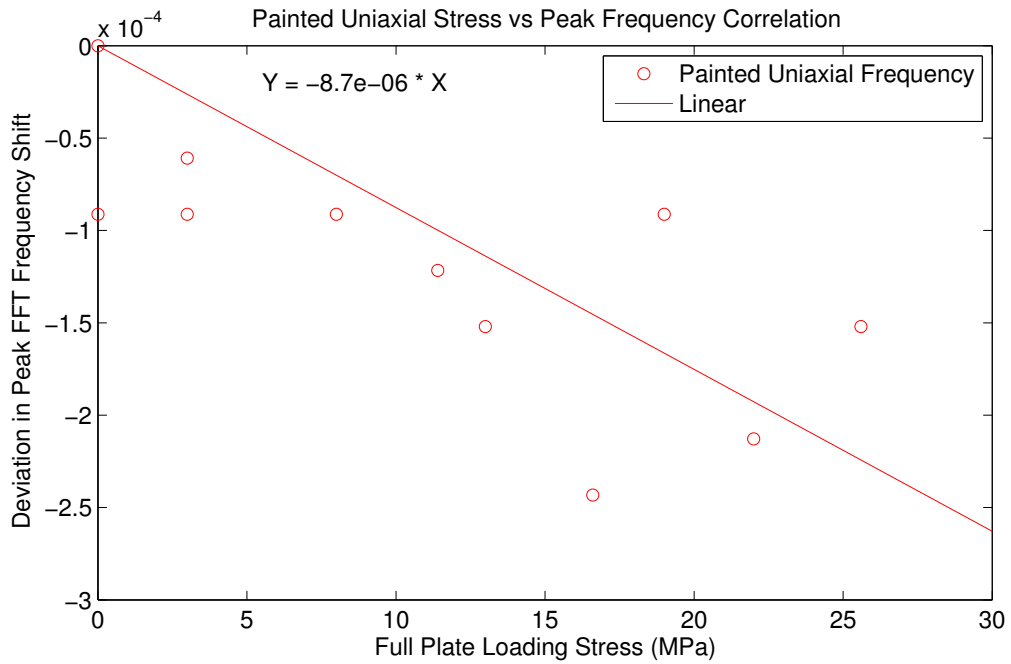


Figure 26. Painted Uniaxial Stress vs. Peak Frequency

TABLE VI

Summary of Uni-Axial Frequency - Stress Correlation Results

Test Detail	Loading Method	Frequency Correlation Slope
Reference	Uniaxial	1.17E-05 (velocity)
Numerical	Uniaxial	-4.2E-06
'L' Shape	Uniaxial	-8.50E-05
0.375 in. Plate	Uniaxial	-5.40E-05
Painted Plate	Uniaxial	-8.70E-06

brush application along with the use of no thinning agent in the paint provide this calibration as a worst case paint condition.

The results are presented in Table VI for the three experimental uni-axial tests. All experimental tests agree with the decreasing frequency trend calculated previously in the numerical studies. Fortunately, the magnitude of the slope in the unpainted experimental study is larger than the numerical study by a factor of 17 times. This increase in slope makes the percent change per unit of stress larger than the corresponding reference velocity measurements. The results from the painted study uncover an additional variable that will need to be addressed on a site by site basis discussed in detail in Chapter 5. The paint application method, thinning amount and number of layers are only a few of the many site characteristics. All of these characteristics must be factored into using a paint verses using a non-painted frequency stress relationship slope.

#### 4.4 Biaxial Load Study

In order to apply the Rayleigh wave arrival stress identification method to critical structural members, a complex loading scenario must be simulated. To accomplish this complex loading scenario the plate was mounted in a biaxial loading machine. The method of mounting the plate was identical to the uni-axial method with the addition of one more direction of load. A figure presenting the mounting and measurement setup is provided in Figure 27. The general equation of the acoustoelastic velocity effect in a biaxial stress solution is covered by Jassby (Jassby and Saltoun, 1981). Equation 4.2 provides two material-dependent stress acoustic coefficients  $K_1$  and  $K_2$ . Based on the analytical solutions, the shear stress is noted as having no effect on the Rayleigh stress wave propagation. In the biaxial study, Equation 4.2 will be modified to solve for deviation in frequency  $\frac{(f-f_0)}{f_0}$  instead of velocity.

In previous applications only uniaxial machines were used in published biaxial testing. To obtain the second coefficient in previous publications the wedge device would be rearranged perpendicular to the loading. The first goal of biaxial testing is to measure  $K_1$  and  $K_2$  in the frequency domain at multiple biaxial load stages without rearranging the device. The second goal is to compare the parallel measured result against an angled measuring orientation to simulate field plate stress measurements.

$$\frac{(v - v_o)}{v_o} = K_1 * \sigma_{11} + K_2 * \sigma_{22} \quad (4.2)$$

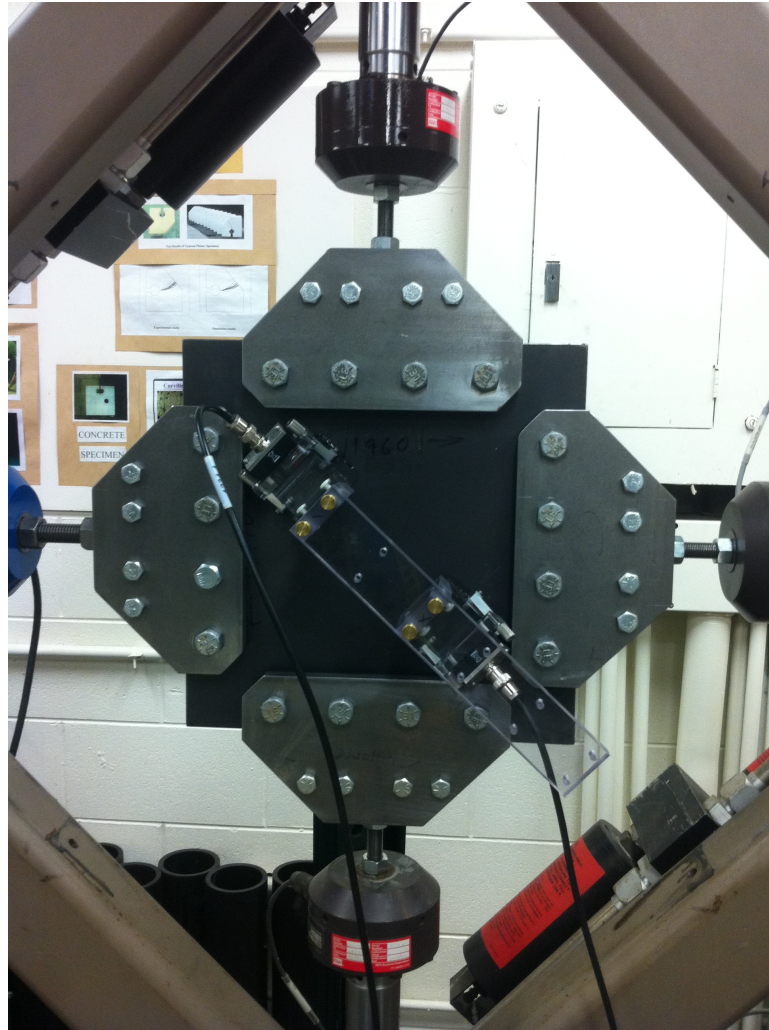


Figure 27. Plate Mounted in Biaxial with Sensor Aligned on Angle

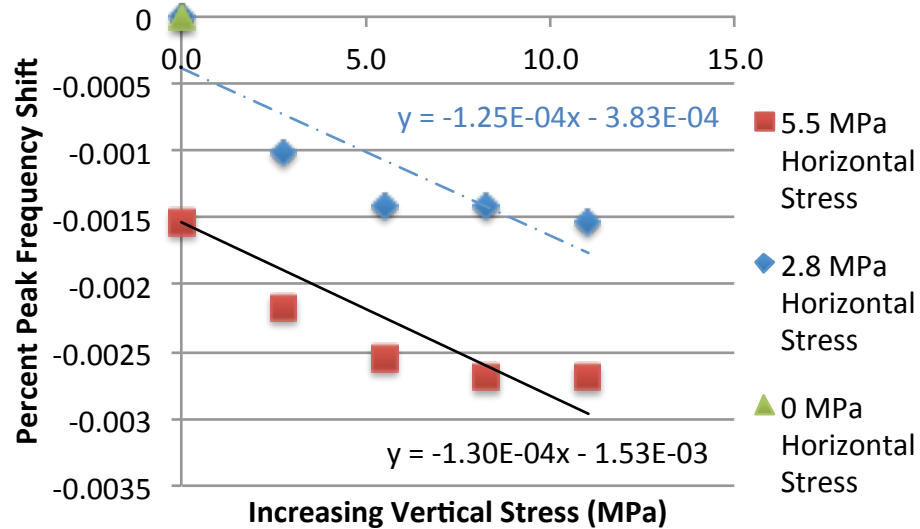


Figure 28. Biaxial Measurement Result Parallel with Vertical Loading Reference

#### 4.4.1 Painted Plate, Measurement Parallel with Vertical Loading

The first biaxial test is performed on a 0.375 in. (9.2mm) painted plate. The sensor handle was placed parallel with the direction of the vertical applied loads. The method of loading started with zero load, then set a horizontal load of 5 KN and step increased the vertical loading from 0 - 20 KN. Waveforms were saved at each load step. The horizontal loading was then increased to 10 KN and the vertical loading was step increased again. The initial measured data plotted against the increasing vertical loading is provided in Figure 28.

The vertical load (parallel to sensor) and horizontal load (perpendicular to sensor) directions will be defined as directions 1 and 2 respectively. From this loading scheme,  $K_2$  from Equa-

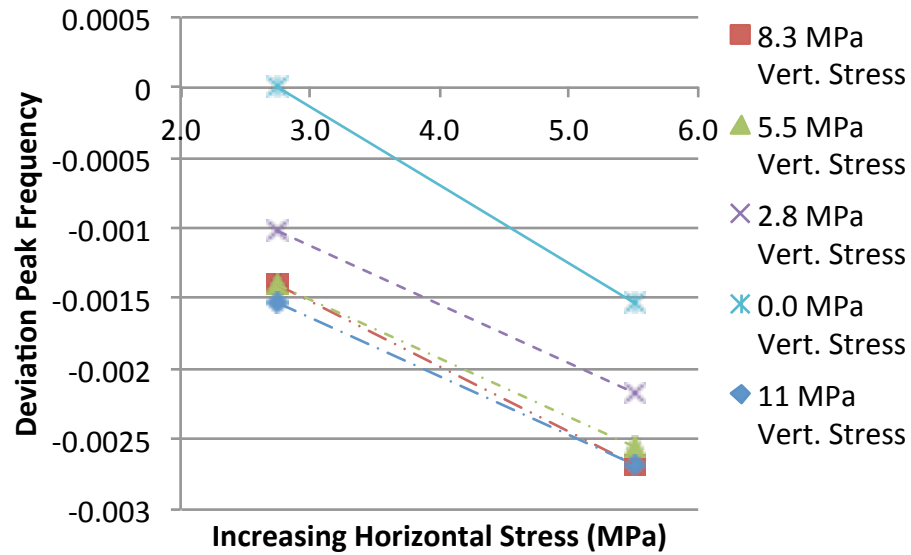


Figure 29. Biaxial Result Sensor Parallel with Vertical Loading Reference

tion 4.2 can be defined by the average slope between equivalent vertical stress ( $\sigma_1$ ) stages at different horizontal ( $\sigma_2$ ) stages. A plot of the two horizontal stress steps and resulting measured frequency is presented in Figure 29

The consistent change in frequency deviation as an isolated result of increased horizontal stress supports the relationship suggested by Equation 4.2. The relationship of each load step was averaged to provide  $K_2 = -4.54E-04 \frac{1}{MPa}$ . With Equation 4.2 and the first coefficient calculated, the effect of horizontal stress can be removed from the original frequency measurement. From the resulting adjusted frequency we can solve for  $K_1$  based on the remaining slope. Figure 30 presents the adjusted frequency leaving a slope of  $K_1$ .

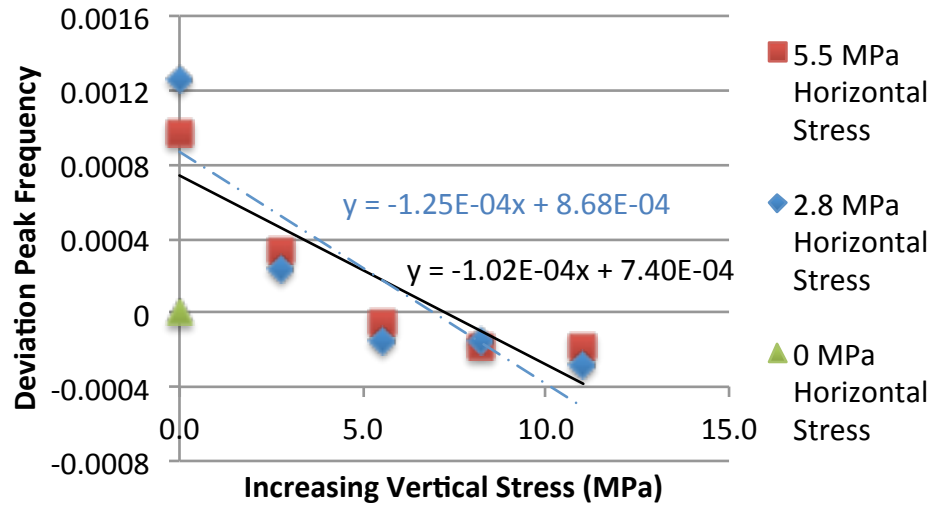


Figure 30. Biaxial Result Parallel with Loading Vertical Loading Reference - Horizontal Stress Effect Removed

The average slope of  $K_1$  in the parallel loading and sensing biaxial test was calculated as  $K_1 = -1.14E-04 \frac{1}{MPa}$ . Visually, from Figure 30, it is evident that the application of the horizontal coefficient brought the two test datasets to a factor of a uniform vertical coefficient,  $K_1$ . This result confirms previous velocity-based testing carried out in uniaxial loading machines. The combined biaxial deviation of frequency is shifted by two linear coefficients when the sensor is placed parallel or perpendicular to the loading directions. The next step was to confirm the biaxial results with an angled measurement direction that will include shear stress, similar to in-situ gusset plates.

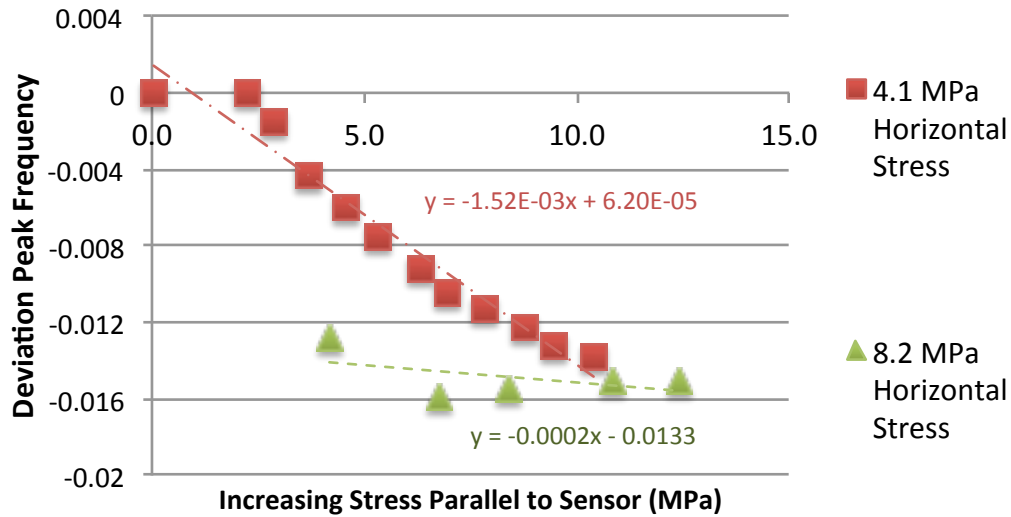


Figure 31. Biaxial Result Angled  $45^{\circ}$  from Loading Reference

#### 4.4.2 Unpainted Plate, Measurement 45 Degree With Vertical Loading

The biaxial angled confirmation test was performed at a approximately  $45^{\circ}$  angle to the loading directions. The angled horizontal and vertical normal stresses were then calculated according to the sensors orientation. The angled measurement configuration is captured in Figure 27. To increase the total stress in the plate, a 0.25 in. (6.4 mm) thick plate was used. Since only the deviation in peak frequency is used, expected full Rayleigh wave penetration frequency shift will be neglected in comparisons. In contrast to the previous biaxial test, the plate used for the angled measurement was not painted during this test.

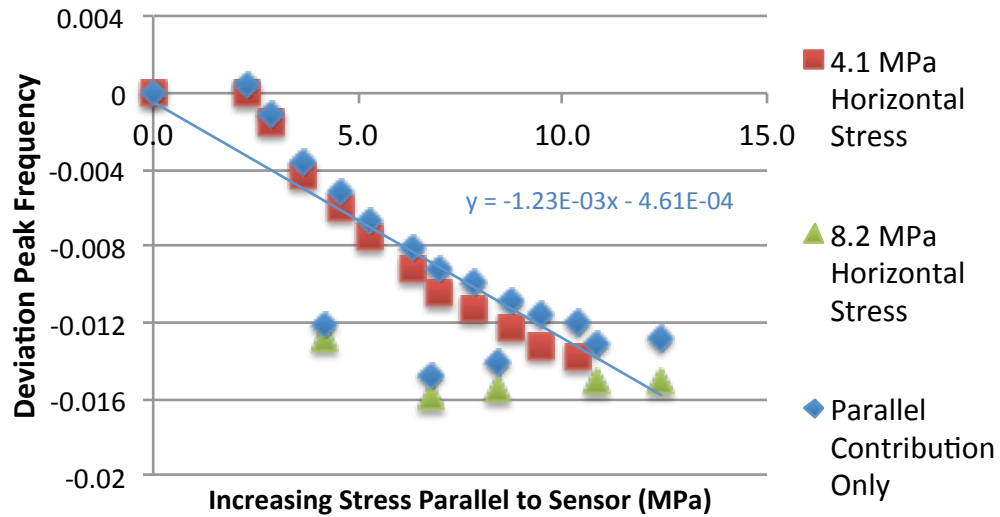


Figure 32. Perpendicular Stress Effect Removed Biaxial Result Angled  $45^{\circ}$  from Loading Reference

The results of the biaxial angled test are presented in Figure 31. In further angled notation the sensor was rotated  $-45^{\circ}$  with the resulting sensor directions 1 and 2 correspond to parallel and perpendicular to the sensor respectively. In contrast to the tests where loading and measurement were parallel, in the angled loading no two measurements have identical loading in a similar relative sensor direction. The combined loading limitation removed a simplistic way to extract  $K_2$  from the combined Equation 4.2. In testing, a curve fit was constructed in Excel to solve for  $K_1$  and  $K_2$  at the same time. The fit was seeded with the painted values for  $K_1$  and  $K_2$ .

The solved values of  $K_1$  and  $K_2$  for a unpainted plate are  $-1.23\text{E-}03 \frac{1}{\text{MPa}}$  and  $-1.72\text{E-}4 \frac{1}{\text{MPa}}$  respectively. As the sensor was rotated the value of  $K_1$  increased as compared to the parallel loading direction biaxial test results. The next step was to apply the  $K_2$  to remove the perpendicular contribution to the frequency deviation and confirm the remaining data followed a linear slope equal to  $K_1$ . The results of the second plate biaxial frequency deviation tests after removal of the perpendicular stress contribution are presented in Figure 32.

As a check on the curve fit method of obtaining the  $K$  coefficients, the slope of the parallel stress should be the same as the solved value of  $K_1$ . The slope of the parallel stress is  $-1.23\text{E-}3 \frac{1}{\text{MPa}}$  in Figure 32 while the curve fit obtained value of  $K_1$  ( $1.23\text{E-}3 \frac{1}{\text{MPa}}$ ). The two values are similar, confirming that the perpendicular component of stress was removed with the obtained  $K_2$  value. Unlike the previous parallel biaxial test Figure 30, the two separate increasing horizontal load steps do not align to a uniform single linear dataset along the parallel component of stress with the perpendicular component removed. This lack of conformity points to a possible additional term missing from Equation 4.2. One possible source for the additional term is the shear stress. This result may contradict previous derivations of the complex loading effect. To properly correct angled frequency measurements to the corresponding stresses the remaining factors will need to be identified. Moving forward we will use the two sets of  $K$  coefficients as a painted and not painted reference.

#### 4.5 Summary

The results of all laboratory tests are provided in Table VII. The primary goal of laboratory testing was to establish a baseline stress-induced frequency shift in the frequency domain of a perturbation.

The first task of identifying potential coupling errors and designing a method to mitigate the influence was accomplished. The two methods of cleaning the surface and wiping excess couplant aided in reducing error during all applicable subsequent tests. Secondly, the method of measuring recoupling deviation as a factor of the pulse-echo frequency shift provides tools to calibrate a grouping of distinct couplings. This method is severely limited by the site-by-site structural symmetry, but overall allows for a basis of error reduction. General improvement of the deviation in sampling as a result has been confirmed on multiple occasions.

The initial uniaxial tests confirmed the general trend of the numerical studies' calculated frequency shift. The uniaxial studies found an increased rate of change for the frequency domain when compared to the literature reference velocity change. In the uniaxial studies, the effect of painting was measured and found to decrease the rate of change for the frequency shift. These measurements provide a boundary for the effect of paint on the stress frequency correlation.

The biaxial tests provided three critical results for the application of the stress measurement device. The first result is that in a bi-axial loading situation the stress frequency relationship has a larger slope than in a uniaxial loading situation. The second result is that in order to accomplish detection of a complex load, at least two measurements are needed perpendicular to each other to solve for  $\sigma_{11}$  and  $\sigma_{22}$ . The third result is that in a case with a unknown

TABLE VII

Summary of Frequency - Stress Correlation Results

Test Detail	Loading Method	Frequency Correlation Slope
Reference	Uniaxial	-1.17E-05 (velocity)
Reference	Biaxial $K_2$ (Aluminum)	-1.09E-06(velocity)
Reference	Biaxial $K_2$ (Al.)	-7.30E-07(velocity)
'L' Shape	Uniaxial	-8.50E-05
0.375 in. Plate	Uniaxial	-5.40E-05
Painted Plate	Uniaxial	-8.70E-06
Painted Plate	Biaxial Parallel $K_1$	-1.14E-4
Painted Plate	Biaxial Perpendicular $K_2$	-4.54E-4
0.25 in. Plate	Biaxial 45 <sup>0</sup> Parallel $K_1$	-1.23E-3*
0.25 in. Plate	Biaxial 45 <sup>0</sup> Perpendicular $K_2$	-1.72E-3*

\* Results do not signify a linear response

loading direction an additional variable such as shear stress may be required to determine the combined stress frequency correlation.

The laboratory results were successful in identifying the slope of the stress frequency linear regression for multiple cases. Further research is needed to clarify the complex loading angled measurement correlation. The next stage is to take the acquired knowledge to a field study and implement methods of application.

## CHAPTER 5

### FIELD DEMONSTRATION

The final component of this investigation is a field based test to validate the approach on a typical fracture critical truss bridge. The purpose of this test is to observe, measure and correlate the results. Observations will be made of the field conditions and limitations. Measurements will be attempted with wedge transducers using the through transmission method. Finally, the measurements will be correlated with a potential stress states using the results of the laboratory scale experiments.

#### 5.1 Bridge Overview

The field process began by sourcing an available bridge from the Illinois Department of Transportation. The fracture critical truss bridge selected was a Pratt Truss bridge. The bridge was originally constructed in 1931 with a total truss span of 227.5 ft (69.3 m) and a width of 56 ft (17.1 m). The bridge spans the Calumet River allowing Halsted Street to flow with unabated 4 lanes of traffic. The bridge is located at approximately south 131st street. The foundation of the truss is provided by a concrete column based at the water edge spanning the width. The region of interest for the Illinois Department of Transportation is the gusset plate (L10) directly above the columns. Access to the bottom side of the truss was provided by an inspection trolley directly underneath the lowest chord. The trolley access was critical in obtaining the ability to reach the gusset plate.

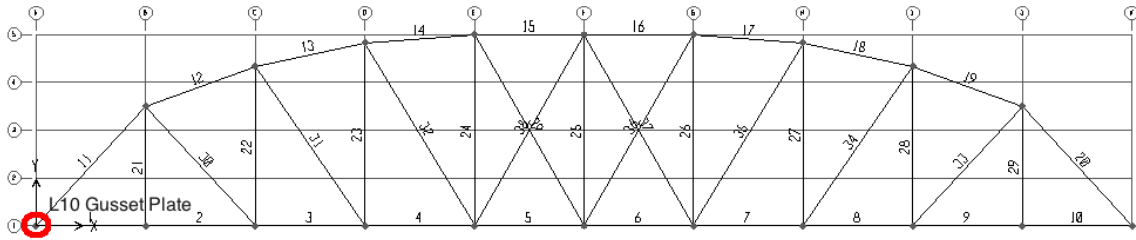


Figure 33. SAP2000 Bridge Overview

## 5.2 Numerical Gusset Plate Solution

Initially, a finite element model was constructed in SAP2000 to observe the entire structural loading of the bridge. The SAP2000 model was constructed by generating the weight and properties of each build-up shape. A reference figure for the full structure model is provided in Figure 33.

Next the resulting loads from the full structure were integrated into a finite element model of the target gusset plate. A drawing of the gusset plate is provided in Figure 34 with the target measurement points labeled. The dead loads carried by each truss element connected to the gusset plate are provided in the drawing. The loads used for this project are based upon the bill of materials within the set of historical drawings. First, the longitudinal members were constructed and a weight generated. Then based on the general structural drawings the remaining total weight was distributed evenly over the structure. Details of the load construction and distribution are captured in Appendix A. The support joint contains a gusset plate on each

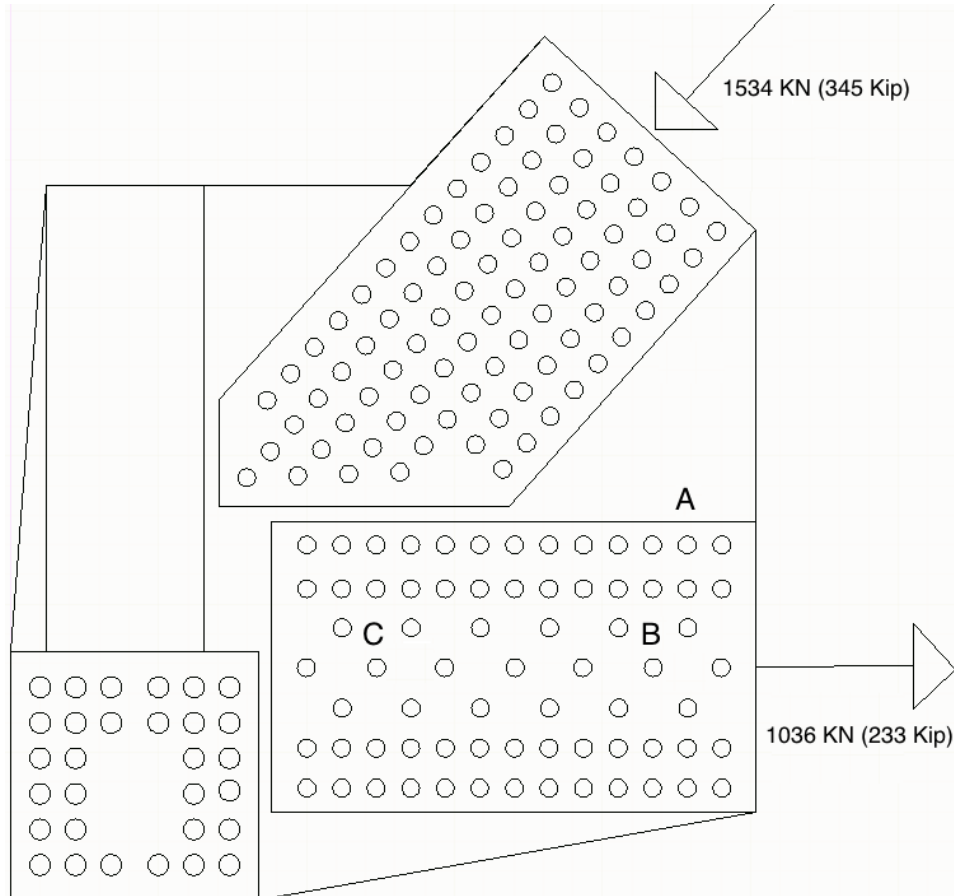


Figure 34. Side Picture of L10 Gusset Plates Connection

side so the SAP2000 joint loads are divided equally between the plates. Special attention was paid to the rivet locations and numerical counts to best match the field conditions.

The generated drawing of the gusset plate was imported into the COMSOL modeling environment. Methods for numerical model construction were based upon relevant developing publications (Liao et al., 2011). A COMSOL finite element solution was constructed to pro-

vide details on the complex loading responses of the gusset plate. To model the proper stress response the boundary conditions were assigned as an axial displacement along the  $43^{\circ}$  vertical member and a simulated pin connection. The simulated pin connection fixed the center of the bottom left connection and distributed the resulting forces to the relative surrounding rivets. This pair of boundary conditions allowed for plate expansion on all of the member connections. The vertical local deck connection was removed from the model due to the low relative load and to reduce the model complexity.

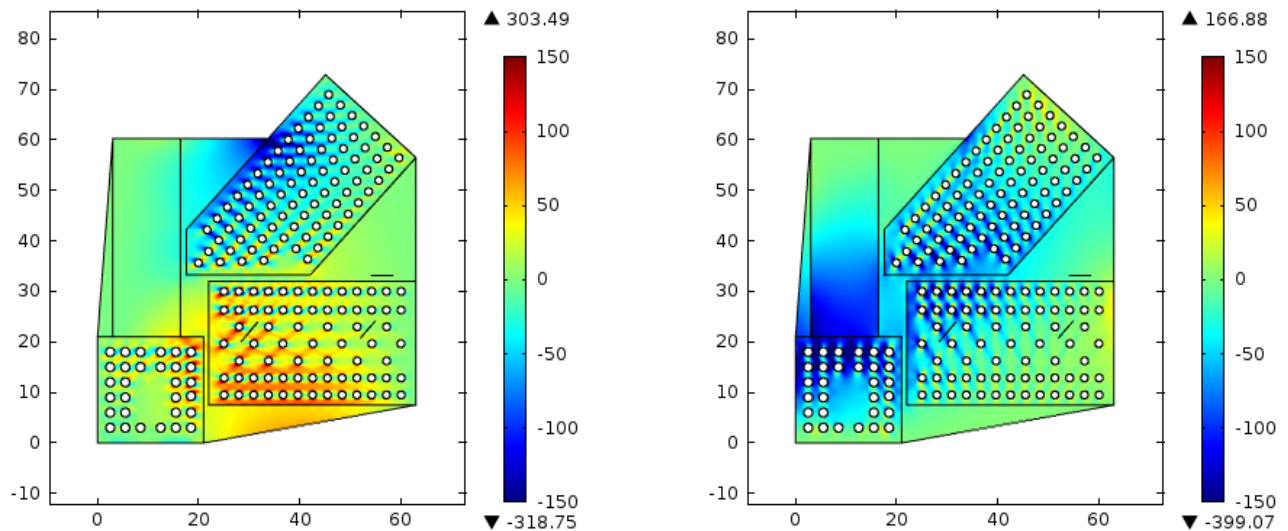


Figure 35. Gusset Plate Numerical Model Stress Solution  
 A) Horizontal Normal Stress Model, B) Vertical Normal Stress Model (MPa)

TABLE VIII

Finite Element Stress Solution to Gusset Plate L10

Location	$\sigma_x$ Horz. MPa	$\sigma_y$ Vert. MPa	$\sigma'_{Perpendicular}$ Sensor Orientation MPa	$\sigma'_{Parallel}$ Sensor Orientation MPa
A	5.6	-8.84	5.6	-8.8
B	12.8	-2.3	5.8	4.6
C	26.0	-52.48	-68.5	42.1

The results of the finite element model are presented in Figure 35. The graphical model shows a region of higher magnitude stress extending off of the fixed pin at a 45 degree angle through the bottom chord connection towards the angled chord. The region directly around the fixed pin rivets may be artifacts of the constrained boundary condition placed on the rivets. Table VIII provides a relevant summary of the solved stress tensor. The placement of sensor locations was designed to provide one low stress region and one complex high stress region. The finite element model presented confirms that the sensor placement was in a mixture of high stress and low stress regions.

Using the results from the finite element model the next step is to provide measurements directly off the L10 gusset plate and compare.

### 5.3 Ultrasonic Measurement

To provide a field measurement the following procedure was followed. A picture of the gusset plate region is provided in Figure 36, with visible identical plates on both sides of the joint. To maximize the benefit of available loading symmetry with a gusset plate on each side of the



Figure 36. Gusset Plate L10 on Field Bridge

beam, measurements were taken at the same locations on each side. Also, to minimize possible human error, a magnet mounting bracket was constructed for the wedge holder. The magnet mount was tested in the laboratory and found to have no noticed effect on the piezoelectric transducer responses. Photos of the sensor coupled to the gusset plate are provided in Figure 37.

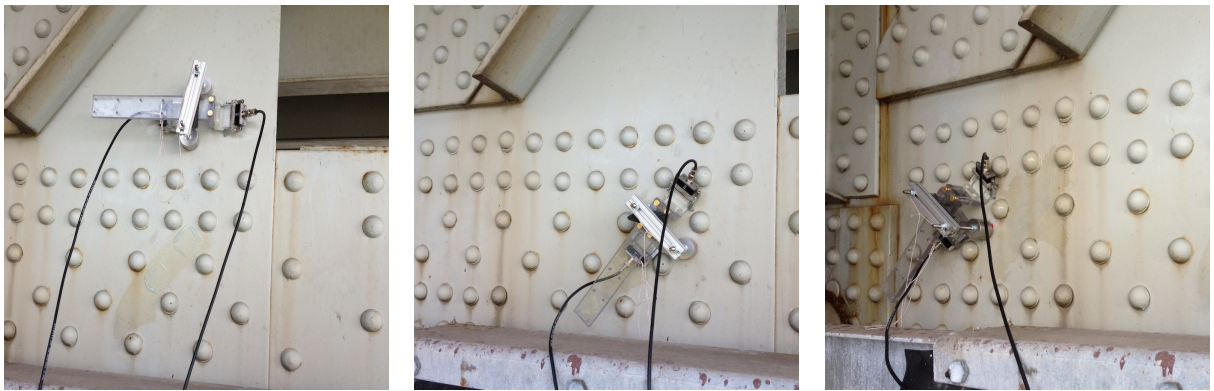


Figure 37. Coupled Ultrasonic Wedge Sensor in Positions A, B, C Respectively

The first stage of measurement was cleaning the surface. The surface preparation began with degreasing spray, followed by wiping an application of couplant. With the surface wiped clean the couplant was applied to the bottom of the wedges and applied to the surface with magnetic force. After application to the plate, the wedges were inspected for any visual contact abnormalities. If abnormalities were found, the process was repeated.

Once the transducers were coupled, a series of three waveform measurements were performed: pulse-echo transmit wedge, pulse-echo receive wedge and a through transmission. For each waveform measurement three files were recorded for averaging and confirmation. It is important to note that the traffic load was varying during the measurement. Multiple measurements from a given location minimize the effect of traffic load on the ultrasonic measurement to identify the dead load stress. This process was repeated for both sides of the gusset plate. The three trial critical variables in the through transmission mode are transmitter coupling, stress frequency shift and receiver coupling. Due to symmetry, the stress frequency shift is constant between the two measurements, then the remaining change in waveform frequency is resulting from the coupling condition. Using the additional pulse-echo tests, the coupling factors can be reduced using the same method as presented in Chapter 2.

Upon inspection, the paint coating applied to the bridge was observed to be thinner than the laboratory painted sample. The primary reasons suspected are the application by a spray brush by the contractors and possible additional paint thinning agents. A similar scenario is expected at each possible field implementation site. Each site paint characteristics are based on the local standard set of protective painting specifications. Visually, the roughness was found to be approximately half way between the laboratory painted and unpainted samples.

To calibrate and compensate for the effect of the paint, a method of determining the extent of the dampening effect is needed. One method that was attempted in this study and provided logical results was to compare initial pulse-echo decay rates. The logic behind this method being that the majority of the difference in energy loss between the similar plates in a short

duration pulse-echo occurs at the boundaries. This energy loss at the boundary will capture a quantitative result of possible paint condition.

A pulse-echo test was performed on a typical section of the field gusset plate and also upon each of the painted and unpainted samples in the lab. The results are presented in Figure 38. The slope of the field painted bridge decayed within the bounds of the two laboratory samples. This confirmed the estimation that the field paint application has a more mild effect on ultrasonic propagation than the laboratory paint application. The linear difference between slopes generates that the field painted sample is approximately 40% as damping as the laboratory painting. This result agrees with the obtained visual approximation for the difference between samples. For the remaining stress identification calculations K1 and K2 will be constructed based on a 40% painted reference and a 60% unpainted reference.

Since according to the finite element model the stress solution is complex in the plate loaded biaxially, two frequency measurements are needed perpendicular to each other. During the field trip, measurements were only taken on one vector in the steel. To compensate for the limitation, the finite perpendicular stress will be used and the parallel stress will be solved.

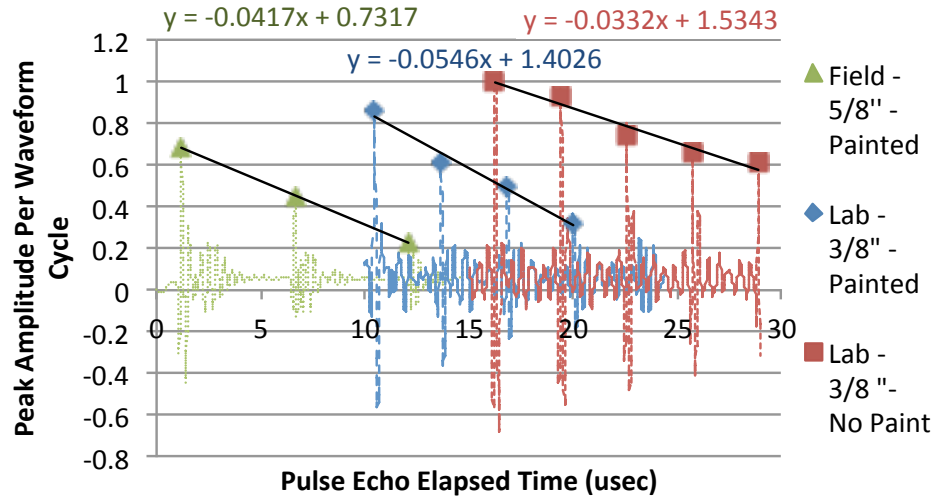


Figure 38. Field Painted, Lab Painted and No Paint on Pulse-Echo Rate of Decay

#### 5.4 Ultrasonic Results

The peak Rayleigh wave frequencies obtained from six measurement locations using through transmission mode are provided in Figure 39. The pulse-echo approach discussed in Section 5.3 to reduce the coupling error is applied to the data and presented in Figure 40. Reducing the coupling error in the field measurement is a critical factor, especially as the ultrasonic frequency shift with stress is relatively weak. In the uncorrected field measurements, Figure 39, no consistent frequency shift per measurement location is obtained. From the corrected measurements, the peak frequencies at the symmetric measurement points are very close to each other. Additionally, the measurement points C1 and C2 are located at the highest stressed

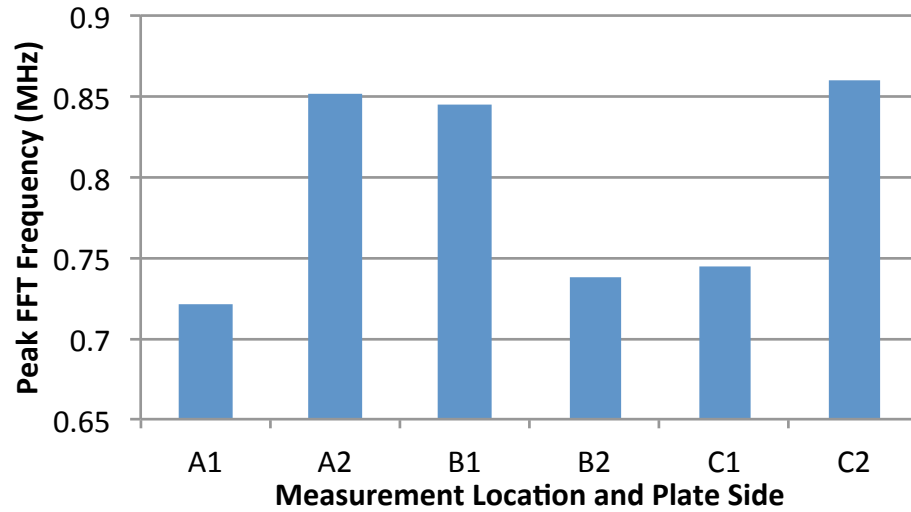


Figure 39. Through Transmit, Uncorrected Measurements

points of the gusset plate and the peak frequencies obtained from these points are the lowest, which agrees with the theory.

The final calculated results using the field paint modified K1 and K2 are presented in Table IX. The results agree in a general increasing trend between points A and C, that is confirmed within the finite element model. In Table IX the range of error between the finite element solution and the measured was between 54% to 254%. One of the best results came from the region of the plate that had the largest principal stresses.

From these field results multiple issues relating to accuracy and repeatability have been uncovered. The increased shear stress present in the field gusset plate may have an additional role upon the individual acoustoelastic coefficients. The increased loss of accuracy at the lower stress regions of the plate may also be a factor of the additional non-linearity of the stress frequency calibration curves. Also, finite element modeling of in-situ gusset plates is still a

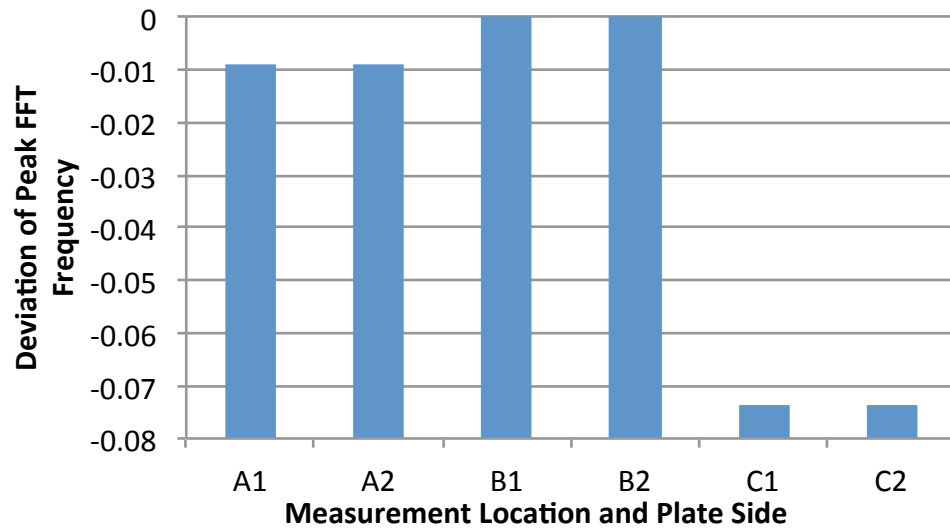


Figure 40. Through Transmit, Pulse-Echo Adjusted Measurements

developing research topic, error within the model and inputs is another region of inaccuracy.

TABLE IX

Measured Solution to Gusset Plate L10

Combined 60/40 Field Coefficients	
$K_1$	-7.84E-04
$K_2$	-2.85E-04

Location	$\frac{(f-f_0)}{f_0}$	$\sigma_{22}^{Finite}$ (MPa)	$\frac{(f-f_0)}{f_0} - K_2\sigma_{22}$	$\sigma_{11}^{Estimated}$ (MPa)	$\sigma_{11}^{Finite}$ (MPa)	% Difference
Point A	-0.009	5.6	-0.011	13.5	-8.8	254%
Point B	0.000	5.8	-0.002	2.1	4.6	54%
Point C	-0.074	-68.5	-0.054	69.3	42.1	-65%

## 5.5 Summary

The field measurements were completed with all three goals being reached during this phase of testing. The first goal was to observe the working conditions present for a standard field gusset plate. The primary result from observations was that variation in paint plays a large role and must be measured and adjusted for on a site by site basis.

The second goal of the field measurements was to attempt to measure through transit waveforms on the surface of an installed gusset plate. The challenges of this goal resulted in successful use of the magnetic wedge mount and positive use of the pulse-echo calibration method.

The final goal of the tests was to correlate the measured frequency deviation with a finite element model. From the raw measurements, correlation was not found until the pulse-echo

adjustment was applied. Once the pulse-echo adjustment was applied, the general trend of the frequency deviation was found to agree roughly with finite stress models. The accuracy of the correlation was found to be at best 54%. Issues suspected to be behind the error were low stress non-linearity, gusset plate model accuracy and additional shear stress acoustoelastic terms.

## CHAPTER 6

### CONCLUSION

#### 6.1 Summary

Stress identification within existing structures is a critical field of research for the existing aging infrastructure network. The general purpose behind the research presented in this thesis is to provide a quantitative window into fracture critical steel gusset plates. The ability to understand existing loads and determine unexpected changes in loading is critical to the long term safety and stability of these structures. Through the acoustoelastic properties of steel the method of ultrasonic stress identification has been explored. The purpose of this research was to further the understanding of the acoustoelastic response in the frequency-domain. Prior surface wave stress frequency calibrations were not able to be found in published literature.

#### 6.2 Findings

The first stage was to provide a numerical basis of the acoustoelastic effect for the ultimate design of a handheld device. Numerical models were constructed to confirm the frequency-thickness relationship of Rayleigh surface waves and estimate the frequency-stress correlation. The thickness relationship numerical models were designed to provided bounds to select the optimum ultrasonic frequency. The frequency-stress correlation model provided a scope to the expected stress frequency shift. With this scope during initial project reviews, potential sources of errors were flagged and focused on.

The first task of generating suitable experimental stress frequency calibration curves was taken in multiple steps. With each test increasing knowledge about the behavior of each of the testing parameters developed. The coupling conditions were found to be a critical factor and required developing a method of quantitative adjustment. The pulse-echo method of calibration was constructed to allow adjustment for coupling abnormalities. Used in areas of symmetry or similar loading, this method proved to consistently reduce coupling errors. The remaining factor of paint thickness was addressed by generating multiple pairs of coefficients, one for each paint case. The last factor of thickness was resolved to behave precisely as the numerical model calculated.

With the fundamental uniaxial process captured, the focus of investigation turned to application restrictions. Installed steel gusset plates are not ideal uniaxial structures with free surfaces. Further load testing was performed to determine the biaxial response of the frequency stress correlation. Previously no surface wave acoustoelastic publications have contained simultaneous two-direction loading waveform measurements. The published acoustoelastic stress velocity theory resolved the stress frequency relationship when the loading was applied parallel with the coupled sensor. In pursuit to model an arbitrary angle as experienced in the field, the acoustoelastic stress velocity theory failed to provide a satisfactory explanation for the entire frequency shift experienced.

Progressing beyond the laboratory, a field test was procured and measurements were performed upon a 1931 Pratt Truss bridge. A fracture critical gusset plate was flagged to be measured. A numerical model was constructed of the bridge along with a focused model of

the gusset plate. Based on the field conditions, two additional factors effecting measurement, paint thickness and constant coupling were identified and mitigated. In order to adjust the laboratory paint coefficients to the field surface, a method of pulse-echo decay was used to determine the percentage of the paint effect. For a uniform coupling over the course of multiple waveform readings a magnetic holder was constructed. Applying the results measured on the plate with the numerical model, the concept of measuring a frequency to determine stress state appears valid. The error compared to the numerical model was found to be a successful result for a the first initial field based direct application. Further refinement of the complex stress correlation will be needed in order to quantify the expected error obtained through this means of measurement.

### **6.3 Future Work**

- *Biaxial Acoustoelastic Effect:*

Ultimately, the resolution of the field measurements depends on the construction of the biaxial acoustoelastic model. The results obtained through measuring the acoustoelastic effect at an angle to the loading directions conflict with the current model. Additional methods for resolving the complex stress acoustoelastic effect will be needed to solve for the original complex loading parameters.

- *Surface/Paint Characteristics Effect:*

The paint effect is a large variable factor to the propagation of ultrasonic stress waves. Within uniaxial testing, paint was found to have almost a 10 times reduction in the stress frequency relationship. In the field application, a pulse-echo decay was used as a method

to justify visual inspection. Further research is needed to justify or replace this method of paint measurement.

## APPENDICES

Appendix A

**FIELD BRIDGE LOAD CALCULATIONS**

## Appendix A (Continued)

### Bridge Weight Breakdown

Total Weights from Set of Plans

Assume (1/3) of the weight exists on the top nodes

<b>Plan Weight of Materials</b>	
<b>Kips</b>	<b>Description</b>
876	Total Road Concrete
45.7	Total Reinforcing Steel
1088	Total Structural Steel
264	Self Weight of All Longitudinal Members (From Model)
824	Resulting Weight of Structural Lateral Members
275	Total Top Node Lateral Weight (1/3)
550	Total Bottom Node Lateral Weight (2/3)
736	Total 1 Side Bottom Node Combined
137	Total 1 Side Top Node Combined
82	Weight for each Bottom Node
15	Weight for each Top Node

<b>Resulting FEA</b>	
Top Chord	691 Kips (Compression)
Bottom Chord	466 Kips (Tension)

<b>COMSOL Inputs</b>			
Top Chord			
Rise	25	ft	
Run	23	ft	
Diag.	33.97	ft	
Top X Input	-234	kip	Each Plate
Top Y Input	-254	kip	Each Plate
Bot. X Input	233	kip	Each Plate

<b>Check</b>	
2010	Total weight of structure Kip
2034	4x SAP2000 Vertical Component
-1.20%	Percent Difference Within Bounds <10%

**Appendix B**

**FIELD GUSSET PLATE FINITE ELEMENT MODEL ADDITIONAL  
FIGURES**

## Appendix B (Continued)

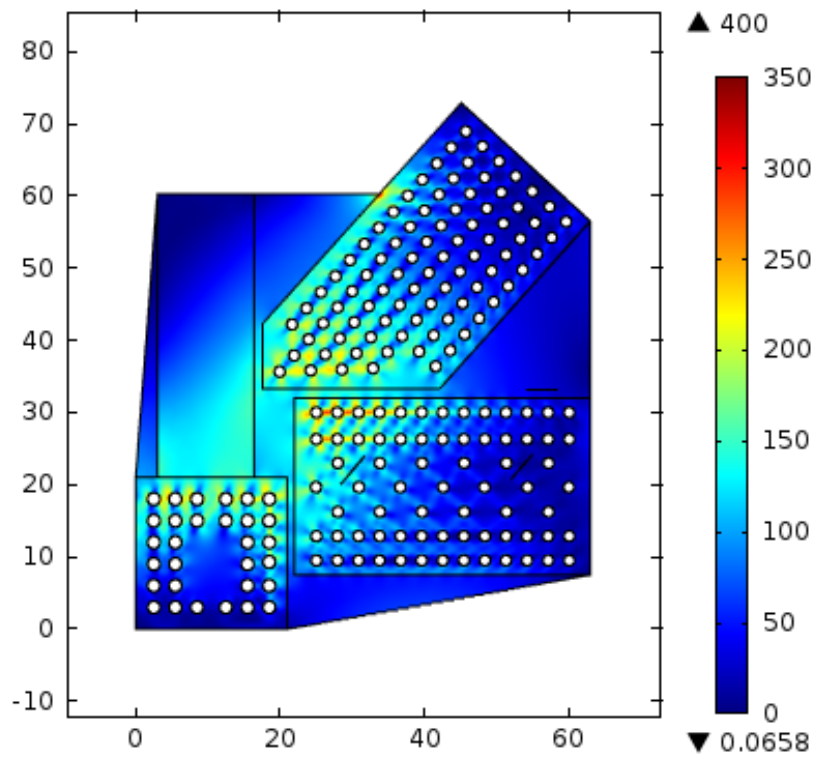


Figure 41. Field Gusset Plate Von Mises Stress (MPa)

## Appendix B (Continued)

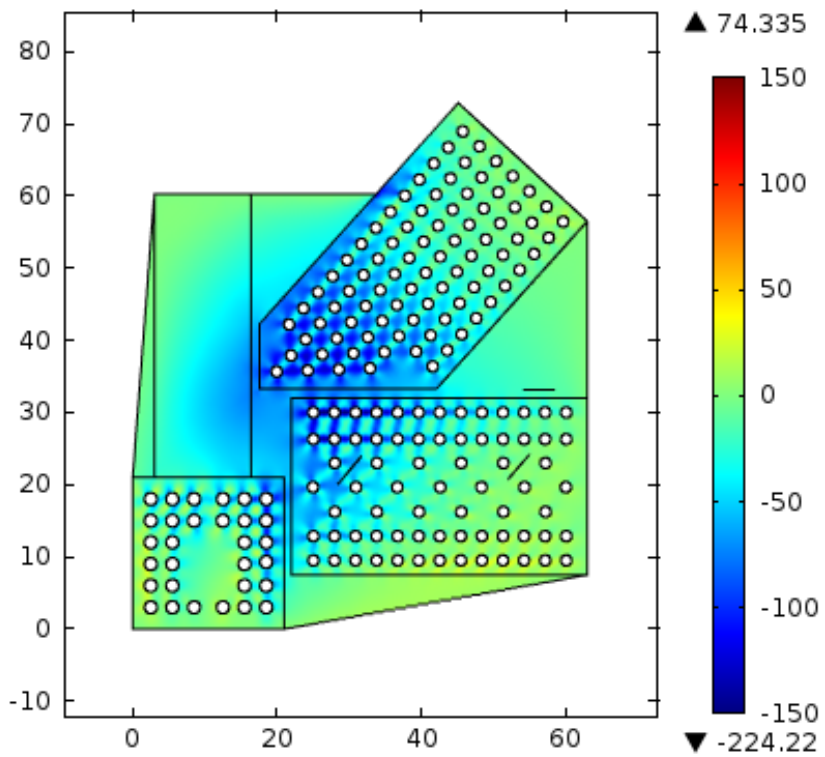


Figure 42. Field Gusset Plate Shear Stress (MPa)

## CITED LITERATURE

- [Achenbach, 1973]Achenbach, J.: Wave Propagation in Elastic Solids. American Elsevier Publishing Company, Inc - New York, 1973.
- [ASM Handbook Committee, 1976]ASM Handbook Committee: Metals Handbook : Nondestructive Inspection and Quality Control , Vol. 11. American Society for Metals, 8th edition, 1976.
- [ASTM, 2010]ASTM: Standard Test Method for Determining Residual Stresses by the Hole-Drilling Strain-Gage Method E837-08, 2010.
- [Berruti, 1996]Berruti, T.: Acoustoelastic Determination of Stresses in Steel Using Rayleigh Ultrasonic Waves, 1996.
- [Chaki and Bourse, 2009a]Chaki, S. and Bourse, G.: Guided ultrasonic waves for non-destructive monitoring of the stress levels in prestressed steel strands. Ultrasonics, 49(2):162–71, February 2009.
- [Chaki and Bourse, 2009b]Chaki, S. and Bourse, G.: Stress Level Measurement in Prestressed Steel Strands Using Acoustoelastic Effect. Ultrasonics, 49(2):673–681, February 2009.
- [Dos Santos and Bray, 2002]Dos Santos, A. a. and Bray, D. E.: Comparison of Acoustoelastic Methods to Evaluate Stresses in Steel Plates and Bars. Journal of Pressure Vessel Technology, 124(3):354, 2002.
- [Egle and Bray, 1976]Egle, D. M. and Bray, D. E.: Measurement of acoustoelastic and third-order elastic constants for rail steel. Journal of the Acoustical Society of America, 60(3), 1976.
- [Gallagher, 2003]Gallagher, K.: Experimental Methods for Measuring the Dead Load Stress in Steel Girder Bridges. Technical report, Rowan University, Glassboro, NJ, 2003.
- [Gokhale, 2007]Gokhale, S.: Determination of applied stresses in rails using the acoustoelastic effect of ultrasonic waves. Doctoral dissertation, Texas A&M University, 2007.
- [Hill et al. , 2004]Hill, R., Forsyth, S., and Macey, P.: Finite element modelling of ultrasound, with reference to transducers and AE waves. Ultrasonics, 42(1-9):253–8, April 2004.

- [Hu et al. , 2009]Hu, E., He, Y., and Chen, Y.: Experimental study on the surface stress measurement with Rayleigh wave detection technique. Applied Acoustics, 70(2):356–360, February 2009.
- [Hughes and Kelly, 1953]Hughes, D. S. and Kelly, J. L.: Second order elastic deformation of solids. Physical Review, 92(5), 1953.
- [Jassby and Saltoun, 1981]Jassby, K. and Saltoun, D.: Use of Ultrasonic Rayleigh Waves for the Measurement of Applied Biaxial Surface Stresses in Aluminum 2024-T351 Alloy. Materials Evaluation, 40(2):198, 1981.
- [Junge, 2003]Junge, M. D. A.: Measurement of applied stresses using the polarization of Rayleigh surface waves.pdf. Doctoral dissertation, Georgia Institute of Technology, 2003.
- [Levy, 2001]Levy, M.: Modern Acoustical Techniques for the Measurement of Mechanical Properties. San Diego, Academic Press, 2001.
- [Liao et al. , 2011]Liao, M., Okazaki, T., Ballarini, R., Schultz, A. E., and Galambos, T. V.: Non-linear Finite-Element Analysis of Critical Gusset Plates in the I-35W Bridge in Minnesota. Journal of Structural Engineering, 137(January):59–68, 2011.
- [Norris, 1998]Norris, A. N.: Finite-Amplitude Waves in Solids. Nonlinear Acoustics, 1998.
- [Peng et al. , 2009]Peng, H., Meng, G., and Li, F.: Modeling of wave propagation in plate structures using three-dimensional spectral element method for damage detection. Journal of Sound and Vibration, 320(4-5):942–954, March 2009.
- [Rizzo and Lanza di Scalea, 2003]Rizzo, P. and Lanza di Scalea, F.: Effect of Frequency on the Acoustoelastic Response of Steel Bars. Experimental Techniques, 0(December):40–43, 2003.
- [Sun et al. , 2006]Sun, L., Kulkarni, S. S., Achenbach, J. D., and Krishnaswamy, S.: Technique to minimize coupling-effect in acoustic nonlinearity measurements. Journal of the Acoustical Society of America, 120(5):2500–2505, 2006.
- [Wardhana and Hadipriono, 2003]Wardhana, K. and Hadipriono, F. C.: Analysis of Recent Bridge Failures in the United States. Journal of Performance of Constructed Facilities, 17(August):144–150, 2003.

[Zeiger and Jassby, 1982]Zeiger, A. and Jassby, K.: Measurement of Acoustoelastic Coefficients of Rayleigh Waves in Steel Alloys. Journal of Nondestructive Evaluation, 3(2), 1982.

## VITA

Mr. James Bittner is currently a Graduate Student in the College of Engineering at the University of Illinois at Chicago. Mr. Bittner graduated Magna Cum Laude from Michigan Technological University with a Bachelors of Science in Civil Engineering. In 2008, Mr. Bittner worked for Great Lakes Dredge and Dock Company estimating land reclamation contracts based upon geotechnical investigations. During this time Mr. Bittner worked with crews to research superior methods of dredge engineering. Ultimately, the research led to the publication of proper field methods for booster placement (Bittner et al., 2011). Mr. Bittner earned a Masters of Science in Civil Engineering from University of Illinois at Chicago in 2012.

[Bittner et al., 2011] Bittner, J., Nelson, J., Rankey, M.: Getting the details right in booster placement. Western Dredging Association (WEDA XXXI) Technical Conference, June 2011